Numerical Analysis and Scientific Computing
Preprint Seria

A higher-order discontinuous Galerkin/arbitrary Lagrangian Eulerian partitioned approach to solving fluid-structure interaction problems with incompressible, viscous fluids and elastic structures

Y. Wang A. Quaini S. Čanić

Preprint #59

Department of Mathematics
University of Houston

April 2017

A Higher-Order Discontinuous Galerkin/Arbitrary Lagrangian Eulerian Partitioned Approach to Solving Fluid-Structure Interaction Problems with Incompressible, Viscous Fluids and Elastic Structures

Yifan Wang, Annalisa Quaini, and Sunčica Čanić
Department of Mathematics
University of Houston

Abstract

This manuscript presents a discontinuous Galerkin-based numerical method for solving fluid-structure interaction problems involving incompressible, viscous fluids. The fluid and structure are fully coupled via two sets of coupling conditions. The numerical approach is based on a high-order discontinuous Galerkin (with Interior Penalty) method, which is combined with the Arbitrary Lagrangian-Eulerian approach to deal with the motion of the fluid domain, which is not known *a priori*. Two strongly coupled partitioned schemes are considered to resolve the interaction between fluid and structure: the Dirichlet-Neumann and the Robin-Neumann schemes. The proposed numerical method is tested on a series of benchmark problems, and is applied to a fluid-structure interaction problem describing the flow of blood in a patient-specific aortic abdominal aneurysm before and after the insertion of a prosthesis known as stent graft. The proposed numerical approach provides sharp resolution of jump discontinuities in the pressure and normal stress across fluid-structure and structure-structure interfaces. It also provides a unified framework for solving fluid-structure interaction problems involving nonlinear structures, which may develop shock wave solutions that can be resolved using a unified discontinuous Galerkin-based approach.

Keywords: Fluid-structure interaction; Discontinuous Galerkin methods; Arbitrary Lagrangian-Eulerian formulation; Domain decomposition methods; Hemodynamics.

1. Introduction

This work is motivated by problems arising in cardiovascular applications where modeling the interaction between the flow of an incompressible, viscous fluid such as blood and an elastic/viscoelastic structure such as cardiovascular tissue or vascular prosthesis is of paramount importance. Sharp resolution of the jump in the normal stress across the fluid-structure interface, or across a structure-structure interface in multi-layered structures, is one of the difficulties associated with the numerical resolution of this class of problems. Notice that the same difficulties arise in many engineering applications, e.g., the interaction between air domes and the surrounding air. The resolutions of sharp jumps across the interface influences the quality of the underlying fluid-structure interaction (FSI) solution, and of the calculation of the biological or physical quantities such as, e.g., wall shear stress. As an example of such a problem, in this manuscript we consider the flow of an incompressible, viscous fluid modeled by the Navier-Stokes equations simulating blood flow through an aortic abdominal aneurism (AAA) before and after treatment with a vascular prosthesis called stent graft. See Fig. 1. AAA is a localized enlargement of the abdominal aorta, which is the largest artery in the human body. See Fig. 1. It is caused by the weakening of the aortic wall, usually caused by atherosclerosis. The pressure exerted by the blood flow onto the weakened and bulged walls of AAA may cause AAA rupture, which may be fatal.

Figure 1: A sketch of AAA treated with a stent-graft (from: www.badaorta.com).

A way to treat AAA entails inserting a vascular prosthesis called stent-graft, shown in Fig. 1, which excludes the aneurysm sack from circulation, and lowers the probability of AAA rupture. It is of particular interest to explore how the pressure on the AAA walls is influenced by the implantation of a stent-graft. The answer to this question depends on the biophysical parameters such as shape of AAA and the elastic properties of the stent-graft material and of the aortic walls. Accurate description of the pressure heavily depends on the accuracy and sharpness of the numerical description of the pressure jump across the stent-graft which divides the flow inside the stent-graft (the lumen) and the fluid occupying the aneurysm sack. A discontinuous Galerkin (DG) method is a way to deal with this difficulty.

We are interested in fluid-structure interaction problems where the location of the structure is not known *a priori*, but is one of the unknowns in the problem, the fluid is incompressible, and the fluid domain is moving in time. This is a nonlinear moving-boundary problem whose resolution has attracted a lot of attention within the past several decades. Most literature reports on the use of either conforming finite elements [4, 75, 16, 15, 20] or finite difference [71, 70] approaches to discretize the problem in space. To capture the motion of the fluid domain, the Immersed Boundary Method [71, 70, 35, 42, 58, 62, 47] and the Arbitrary Lagrangian Eulerian (ALE) method [32, 51, 75, 16, 15, 17, 31, 45, 64] are perhaps the most popular. We also mention an Extended ALE method recently proposed to capture large structural deformations [10], the Fictitious Domain Method in combination with the mortar element method or ALE approach [4, 83], the Lattice Boltzmann method [34, 36, 55, 56], the Level Set Method [29], and the Coupled Momentum Method [40].

In this manuscript we use the *Discontinuous Galerkin with Interior Penalty* method [1, 2, 80] for spatial discretization, and combine it with an Arbitrary Lagrangian Eulerian approach to deal with the motion of the fluid domain. DG methods combined with ALE approaches have been used for the simulation of *compressible Navier-Stokes equations* in moving geometries, see e.g., [59, 69, 25]. Furthermore, DG methods have recently become a competitive choice for solving the incompressible Navier-Stokes equations on fixed domains [27, 39, 81]. Most recently a space-time Hybridizable Discontinuous Galerkin (HDG) finite element method was introduced for problems involving *incompressible Navier-Stokes equations* on moving domains, as an alternative to the ALE method to deal with the dynamically changing, *a priori* given motion of the fluid domain [78]. The HDG approach proposed in [78] has the ability to achieve higher-order accurate approximations in both time and space by simply increasing the order of polynomial approximation in the space-time elements. The problems under consideration in [78], however, included fluid domain motions that are prescribed.

We consider a fully coupled fluid-structure interaction problem, where the structure is elastic (modeled by a couple of different membrane or shell models), the fluid is incompressible, and the fluid domain is moving in time as a function of the structure position. Thus, the structure in this manuscript is a co-dimension one manifold, moving in a way that allows the use of an ALE method (i.e., the ALE mapping is a diffeomorphism). The fluid and structure are coupled via two sets of coupling conditions: the kinematic coupling condition describing continuity of velocity at the fluid-structure interface, and the dynamic coupling

condition describing the balance of contact forces (traction) at the fluid-structure interface. Moreover, since we target cardiovascular applications, we take the structure density close to the density of the fluid, since cardiovascular tissue is composed of mostly water. This is an additional difficulty that needs to be considered in cases when the fluid motion is not prescribed *a priori*, since in such scenarios loosely coupled partitioned (explicit, iterative) schemes suffer from stability issues associated with the so called *added mass effect* [23]. Monolithic algorithms are a way to circumvent this difficulty [40, 45, 64, 85, 13, 12]. These algorithms are based on solving the entire nonlinear fluid and structure coupled problem as one monolithic system. They are, however, generally quite expensive in terms of the computational time, programming time and memory requirements, since they require solving large nonlinear systems using, e.g., the fixed point and Newton's methods [24, 64, 31, 61].

The multi-physics nature of this class of problems strongly suggest to employ partitioned (or staggered) numerical algorithms, where the coupled fluid-structure problem is separated into a pure fluid sub-problem and a pure structure sub-problem [16, 5, 14, 17, 18, 20, 21, 49, 65, 38, 37, 3, 7, 31, 30, 8, 9, 30]. The fluid and structure sub-problems are solved in an alternating way, and the coupling conditions are enforced asynchronously. When the density of the structure is much larger than the density of the fluid, as is the case in aeroelasticity, it is sufficient to solve, at every time step, just one fluid sub-problem and one structure sub-problem to obtain a solution. For problems for which the added mass effect is strongly pronounced, such as cardiovascular applications, sub-iterations at every time step are usually necessary to get a better approximation of the energy of the coupled problem and guarantee stability. We consider in this manuscript two such classical strongly-coupled partitioned schemes: the Dirichlet-Neumann [57] and the Robin-Neumann partitioned scheme [65]. At every time step a fluid and a structure sub-problems are solved with sub-iterations, followed by an update of the current fluid domain, and of the fluid domain mesh. For this purpose an ALE mapping based on the harmonic extension of the boundary data onto the fluid domain is used. It was shown in [52] that this mapping satisfies the *discrete geometric conservation law* associated with nonlinear stability of ALE schemes [60, 19]. The Laplace's equation defining the ALE mapping was solved with the already available DG (with Interior Penalty) approach constructed for the fluid sub-problem.

The *time discretization* is performed using a *second order semi-implicit splitting scheme*, introduced in [44] for fluid problems on fixed domains. See also [50, 76] for more details about this scheme.

In summary, in this manuscript we introduce the first ALE based Interior Penalty Discontinuous Galerkin (IP-DG) strongly-coupled partitioned scheme for solving fluid-structure interaction problems involving incompressible fluids, where a sharp resolution of jump discontinuity across the fluid-structure interface, or within a nonlinear structure, is of particular importance. This IP-DG-ALE based strongly-coupled partitioned schemes is tested on a series of benchmark problems and a real-life inspired problem of blood flow through an aortic abdominal aneurysm. The test problems are as follows:

- *2D and 3D flow past a cylinder [79, 53, 11]*: verifying the accuracy and performance of the fluid DG solver, including mass conservation.
- *FSI benchmark problem of flow through a 2D cylinder with elastic walls [43, 73, 7, 16, 48]*: testing the Dirichlet-Neumann FSI solver.
- *Stationary linearly elastic 1D membrane bubble*: testing the Robin-Neumann FSI solver and showing sharp resolution of pressure jump across fluid-structure interface.
- *Oscillating linearly elastic 1D membrane bubble*: testing convergence of Robin-Neumann FSI solver with respect to mesh refinement, and showing accuracy of mass conservation.
- *Aortic Abdominal Aneurysm with and without a Stent Graft:* 2D and 3D simulations of flow in a patient-specific AAA geometry with elastic walls are presented. In the 2D case the difference in the pressure on the AAA walls was compared before and after the implantation of a stent-graft, showing significant reduction in the pressure and displacement of the AAA walls after the insertion of the stent-graft.

This is the first step toward developing a unified approach based on DG-ALE strongly-coupled partitioned solvers for FSI problems between incompressible viscous fluids and elastic structures. In particular, our goal

is to study FSI problems involving *nonlinearly elastic* structures, where accurate resolution of not only the pressure jump across the interfaces, but also accurate resolution of singularity formation within the nonlinearly elastic structures themselves is of importance.

2. Problem definition

We consider a fluid-structure interaction problem between an incompressible, viscous, and Newtonian fluid and a linearly elastic structure. The fluid domain, which is not known a priori, is a function of time, and is denoted by $\Omega(t) \subset \mathbb{R}^d$, with $d = 2, 3$. The structure covers a part of the fluid domain boundary, denoted by $\Gamma(t)$, and it is assumed to be thin, i.e. $(d-1)$-dimensional. Thus, the structure domain coincides with the fluid-structure interface.

2.1. The fluid equations

The motion of an incompressible, viscous fluid with density ρ and kinematic viscosity ν in a spatial domain $\Omega(t)$, with $t \in (0, T)$, is described by the Navier-Stokes equations

$$\partial_t \boldsymbol{u} + \nabla \cdot \boldsymbol{F}(\boldsymbol{u}) = \frac{1}{\rho}(\nabla \cdot \boldsymbol{\sigma}) = -\frac{1}{\rho}\nabla p + \nu \Delta \boldsymbol{u} \qquad \text{in } \Omega(t), \tag{1}$$

$$\nabla \cdot \boldsymbol{u} = 0 \qquad \text{in } \Omega(t), \tag{2}$$

where $\boldsymbol{u}$ is the fluid velocity, $\boldsymbol{\sigma}$ is the Cauchy stress tensor, which is given by $\boldsymbol{\sigma} = -p\mathbf{I} + 2\nu\rho\mathbf{D}(\boldsymbol{u})$, where $\mathbf{D}(\boldsymbol{u})$ is strain rate tensor,and p is the fluid pressure. We use $\boldsymbol{F}(\boldsymbol{u}) = \boldsymbol{u} \otimes \boldsymbol{u}^T$ to denote the quadratic flux corresponding to the nonlinear advection term $(\boldsymbol{u} \cdot \nabla)\boldsymbol{u}$, which can be written in conservation form $\nabla \cdot \boldsymbol{F}(\boldsymbol{u})$ for an incompressible fluid. This form will be convenient for the presentation of the numerical method in Sec. 4. Equations (1)-(2) are supplemented with the initial data $\boldsymbol{u} = \boldsymbol{u}_0$ in $\Omega \times \{0\}$ and boundary conditions given as follows:

$$\boldsymbol{u} = \boldsymbol{u}_D \qquad \text{on } \partial\Omega_D \times (0, T), \tag{3}$$

$$\boldsymbol{\sigma}\boldsymbol{n} = -p_N \boldsymbol{n} \qquad \text{on } \partial\Omega_N \times (0, T), \tag{4}$$

where $\overline{\partial\Omega_D} \cup \overline{\partial\Omega_N} \cup \overline{\Gamma(t)} = \overline{\partial\Omega(t)}$, $\partial\Omega_D \cap \partial\Omega_N = \emptyset$, and $\boldsymbol{u}_D$ and p_N are given data on the fixed Dirichlet boundary $\partial\Omega_D$ and Neumann boundary $\partial\Omega_N$, respectively. The boundary $\Gamma(t)$ corresponds to the moving structure boundary. The data on $\Gamma(t)$ will be specified below from the coupling conditions between the fluid and structure. We consider the particular Neumann boundary condition in (4) because it is relevant to the applications that will be presented in Sec. 5. We assume that the fluid motion is driven by the boundary conditions (inlet and outlet boundary data) and no external force is applied to the fluid.

The Reynolds number can be used to characterize the flow regime. We define the Reynolds number as

$$Re = \frac{UD}{\nu}, \tag{5}$$

where U is a characteristic velocity magnitude and D is a characteristic length, e.g. U is the mean sectional velocity within a pipe of diameter D. The Reynolds number can be thought of as the ratio of inertial forces to viscous forces. For large Reynolds numbers, inertial forces are dominant over viscous forces and vice versa.

2.1.1. The ALE mapping

In order to describe the evolution of the fluid domain, we adopt an *Arbitrary Lagrangian-Eulerian* (ALE) approach, see, e.g. [51]. Let $\Omega_0 \subset \mathbb{R}^d$ be a fixed reference domain, e.g. $\Omega_0 = \Omega(0)$. We consider a smooth mapping

$$A_t : \Omega_0 \longrightarrow \Omega(t),$$
$$A_t : \boldsymbol{x}_0 \mapsto \boldsymbol{x},$$

where $\boldsymbol{x}$ and $\boldsymbol{x}_0$ are the coordinates in the physical domain $\Omega(t)$ and the reference domain Ω_0, respectively. For each time instant $t \in [0, T]$, A_t is assumed to be a diffeomorphism. The domain velocity $\boldsymbol{w}$ is given by

$$\boldsymbol{w}(t, \cdot) = \frac{dA_t}{dt}(t, A_t(t, \cdot)^{-1}).$$

The ALE time derivative of the fluid velocity is defined as:

$$\partial_t \boldsymbol{u}|_{\boldsymbol{x}_0} = D_t \boldsymbol{u}(t, A_t(\boldsymbol{x}_0)) = \partial_t \boldsymbol{u}(t, \boldsymbol{x}) + \boldsymbol{w}(t, \boldsymbol{x}) \cdot \nabla \boldsymbol{u}(t, \boldsymbol{x}), \text{ for } \boldsymbol{x} = A_t(\boldsymbol{x}_0),\ \boldsymbol{x}_0 \in \Omega_0.$$

With these definitions, we can write the incompressible Navier-Stokes equations in the ALE formulation as follows:

$$\partial_t \boldsymbol{u}|_{\boldsymbol{x}_0} + \nabla \cdot \boldsymbol{F}(\boldsymbol{u}) - \boldsymbol{w} \cdot \nabla \boldsymbol{u} = -\frac{1}{\rho}\nabla p + \nu \Delta \boldsymbol{u} \qquad \text{in } \Omega(t), \tag{6}$$

$$\nabla \cdot \boldsymbol{u} = 0 \qquad \text{in } \Omega(t). \tag{7}$$

Since the time derivative is now computed in the reference domain, the ALE formulation is well-suited for the time discretization.

Let J_{A_t} denote the Jacobian of the deformation gradient, i.e. $J_{A_t} = \det(\frac{\partial \boldsymbol{x}}{\partial \boldsymbol{x}_0})$. We have:

$$\partial_t J_{A_t}|_{\boldsymbol{x}_0} = J_{A_t} \nabla \cdot \boldsymbol{w}.$$

With this notation, we can write the fluid and ALE advection in conservation form to obtain:

$$\partial_t (J_{A_t} \boldsymbol{u})\Big|_{\boldsymbol{x}_0} + J_{A_t} \nabla \cdot (\boldsymbol{F}(\boldsymbol{u}) - \boldsymbol{w} \otimes \boldsymbol{u}^T) = -\frac{J_{A_t}}{\rho}\nabla p + J_{A_t} \nu \Delta \boldsymbol{u} \quad \text{in } \Omega(t). \tag{8}$$

The ALE map can be written in terms of fluid domain displacement $\boldsymbol{d}(\boldsymbol{x}_0, t)$ as $A_t(\boldsymbol{x}_0) = \boldsymbol{x}_0 + \boldsymbol{d}(\boldsymbol{x}_0, t)$. Let $\boldsymbol{\eta}$ be the displacement of the deformable boundary of Ω_0 denoted by Γ_0, i.e. $\boldsymbol{d}(\boldsymbol{x}_0, t)|_{\Gamma_0} = \boldsymbol{\eta}$. Inside Ω_0 the displacement $\boldsymbol{d}$ is arbitrary: it can be any reasonable extension of $\boldsymbol{\eta}$ over Ω_0. A classical choice is to consider a harmonic extension in the reference domain, that is:

$$\Delta \boldsymbol{d} = \boldsymbol{0} \quad \text{in} \quad \Omega_0, \tag{9}$$

with boundary conditions:

$$\boldsymbol{d} = \boldsymbol{\eta} \quad \text{on } \Gamma_0, \tag{10}$$

$$\boldsymbol{d} = \boldsymbol{0} \quad \text{on } \partial\Omega_0 / \Gamma_0. \tag{11}$$

In the following, we will refer to problem (9) as ALE problem.

2.2. The structure equations

We will be using two different thin structure models to describe the elastic behavior of compliant wall: the generalized string model, and the elastic spring model.

To write the two models recall that we use $\Gamma(t)$ and Γ_0 to denote the current structure domain and the fixed reference structure domain, respectively, and $\boldsymbol{x}$ and $\boldsymbol{x}_0$ to denote the respective coordinates. Let $\boldsymbol{\eta} = (\eta_x, \eta_y, \eta_z)^T = \boldsymbol{x} - \boldsymbol{x}_0$ denote the structure displacement from its reference configuration. The elastodynamics of thin structures studied in this manuscript can be generally described by a partial differential equation which is of the following form:

$$\rho_s h_s \partial_{tt} \boldsymbol{\eta} + \mathcal{L}\boldsymbol{\eta} + \gamma \mathcal{V} \partial_t \boldsymbol{\eta} = \boldsymbol{f}_s \quad \text{in } \Gamma_0 \times (0, T). \tag{12}$$

The third term on the left hand side is added to capture viscoelasticity of the structure. Here, ρ_s is the structure density, h_s is the structure thickness, $\boldsymbol{f}_s$ is the force acting on the structure, and γ is a viscoelastic

parameter. The operator $\mathcal{L}$ in this manuscript will be linear, acting on a vector function $\boldsymbol{\eta}$ describing the elastic properties of the structure (coming from the elastic energy), and $\mathcal{V}$ is a linear operator acting on the vector function $\partial_t \boldsymbol{\eta}$ describing the viscoelastic properties of the structure. In general, $\mathcal{L}$ and $\mathcal{V}$ may be nonlinear operators associated with the elastic or viscoelastic energy of the nonlinearly elastic membrane or shell. Below we will specify the different forms of operators $\mathcal{L}$ and $\mathcal{V}$ that we consider here as simple examples. The general approach to solving FSI problems with the IP-DG-ALE methodology proposed here can be applied to more complicated, nonlinear models, and to structures of finite thickness.

We begin with the generalized string model in 1D [75], which can be considered as a special case of a cylindrical shell model studied in [22]. The reference configuration in this case is a cylinder of radius R_0 and length L. Only the displacement in the transversal direction (or vertical direction y) is considered different from zero, while the longitudinal and azimuthal components of displacement are assumed negligible. The model reads:

$$\rho_s h_s \frac{\partial^2 \eta_y}{\partial t^2} + \frac{E h_s}{(1-\nu_s^2)} \frac{\eta_y}{R_0^2} - kGh_s \frac{\partial^2 \eta_y}{\partial x^2} - \gamma \frac{\partial^3 \eta_y}{\partial x^2 \partial t} = f_{s,y} \tag{13}$$

which means that the operators $\mathcal{L}$ and $\mathcal{V}$ are given by:

$$\mathcal{L}\boldsymbol{\eta} = \left(0, -kGh_s \frac{\partial^2 \eta_y}{\partial x^2} + \frac{E h_s}{(1-\nu_s^2)} \frac{\eta_y}{R_0^2}, 0\right)^T, \quad \mathcal{V}\frac{\partial \boldsymbol{\eta}}{\partial t} = \left(0, -\frac{\partial^3 \eta_y}{\partial x^2 \partial t}, 0\right)^T. \tag{14}$$

Here k is the Timoshenko shear correction factor, G is the shear modulus, E is the Young's modulus, and ν_s is the Poisson ratio of the structure. Structure model (13) is endowed with absorbing boundary conditions of first order:

$$\frac{\partial \eta_y}{\partial t} - \sqrt{\frac{kG}{\rho_s}} \frac{\partial \eta_y}{\partial x} = 0 \quad \text{at } x = 0, \tag{15}$$

$$\frac{\partial \eta_y}{\partial t} + \sqrt{\frac{kG}{\rho_s}} \frac{\partial \eta_y}{\partial x} = 0 \quad \text{at } x = L. \tag{16}$$

We will be using this model to test our computational FSI solver.

The second model we consider does not require the structure reference domain to be a cylinder, and the model involves no spatial derivatives and no viscoelasticity. The operators $\mathcal{L}$ is defined as follows:

$$\mathcal{L}\boldsymbol{\eta} = (C_x \eta_x, C_y \eta_y, C_z \eta_z)^T, \tag{17}$$

and viscoelasticity parameter $\gamma = 0$. In this model, x, y and z correspond to three components of the Cartesian coordinates, and constants (C_x, C_y, C_z) are three spring constants. The specific form of these constants will be given in each example.

Model (12),(17) is supplemented with homogeneous Dirichlet boundary conditions:

$$\boldsymbol{\eta} = \mathbf{0} \quad \text{on } \partial\Gamma_0. \tag{18}$$

Most of our numerical FSI examples will be given in 2D. To show the feasibility that our method can be applied to 3D problem, we conclude the manuscript by showing an example of a pressure wave propagating in a 3D, patient-specific geometry of aortic abdominal aneurysm.

2.3. The coupling conditions

The fluid and the structure problems described in Sec. 2.1 and 2.2 are coupled via two boundary conditions:

- Kinematic coupling condition, which describes the continuity of velocity at the fluid-structure interface (no-slip condition)

$$\boldsymbol{u} \circ A_t = \partial_t \boldsymbol{\eta} \quad \text{on } \Gamma_0 \times (0, T); \tag{19}$$

- Dynamic coupling condition, which describes the continuity of the stress at the fluid-structure interface

$$J\,\widehat{\boldsymbol{\sigma}\boldsymbol{n}}|_{\Gamma(t)} = \boldsymbol{f}_s \quad \text{on } \Gamma_0 \times (0,T), \tag{20}$$

where $\boldsymbol{f}_s$ is given by the left hand-side of (12), J denotes the Jacobian of the transformation from Eulerian to Lagrangian coordinates, and $\widehat{\boldsymbol{\sigma}\boldsymbol{n}}|_{\Gamma(t)}$ denotes the normal fluid stress at the deformed fluid-structure interface, which is evaluated with respect to the reference configuration. Vector $\boldsymbol{n}$ is the outward unit normal to the deformed fluid domain.

Coupling conditions (19)-(20) can be written in the equivalent form:

$$\begin{aligned} \alpha_f \boldsymbol{u} \circ A_t - J\,\widehat{\boldsymbol{\sigma}\boldsymbol{n}}|_{\Gamma(t)} &= \alpha_f \partial_t \boldsymbol{\eta} - \boldsymbol{f}_s \quad \text{on } \Gamma_0 \times (0,T), \\ \alpha_s \boldsymbol{u} \circ A_t + J\,\widehat{\boldsymbol{\sigma}\boldsymbol{n}}|_{\Gamma(t)} &= \alpha_s \partial_t \boldsymbol{\eta} + \boldsymbol{f}_s \quad \text{on } \Gamma_0 \times (0,T), \end{aligned} \tag{21}$$

where $\alpha_f > 0$ and $\alpha_s > 0$ ($\alpha_f \neq \alpha_s$) are constants, which we specify later.

3. Partitioned methods for the fluid-structure interaction problem

The FSI problem described in Sec. 2 will be solved using two different partitioned strategies based on Domain Decomposition methods [77]: the Dirichlet-Neumann (DN) and the Robin-Neumann (RN) algorithms. Partitioned method are appealing for solving multi-physics problems such as those discussed in this manuscript, because they allow the reuse of existing solvers with minimal modifications. Because of the modularity of DN and RN algorithms, each physics sub-problem is solved separately, with the coupling conditions enforced in an iterative fashion. In the DN algorithm the coupling boundary condition (19) is imposed at the interface as a Dirichlet boundary condition for the fluid sub-problem, whereas in the RN algorithm the fluid sub-problem is endowed with Robin interface condition (21). In both algorithms, the structure sub-problem is supplemented with the Neumann "boundary condition" (20). Eq. (20) is a proper Neumann boundary condition when the structure is thick; for thin structures eq. (20) prescribes a load on the structure.

To describe the DN and RN algorithms, we introduce the time-discretization step Δt and set $t^n = n\Delta t$, for $n = 1, \ldots, N$, with $N = T/\Delta t$. At every time t^n, the DN and RN algorithms iterate over the fluid and structure sub-problems until convergence. Let k be the index for these iterations.

3.1. The Dirichlet-Neumann method

Assume that Ω^n, A_{t^n}, J^n, $\boldsymbol{u}^n$ and $\boldsymbol{\eta}^n$ are given. The goal is to calculate Ω^{n+1}, $A_{t^{n+1}}$, J^{n+1}, $\boldsymbol{u}^{n+1}$, p_{k+1}, $\boldsymbol{\eta}^{n+1}$ at time t^{n+1}, by using the following iterations in k. Assume that $\boldsymbol{u}_k$, and $\boldsymbol{\eta}_k$ are known, starting with $\boldsymbol{u}_0 = \boldsymbol{u}^n$, and $\boldsymbol{\eta}_0 = \boldsymbol{\eta}^n$. Calculate:

- **Step 1**: Solve the fluid sub-problem for the flow variables of $\boldsymbol{u}_{k+1}$ and p_{k+1} on the fluid domain Ω^n with Dirichlet boundary condition:

$$\boldsymbol{u}_{k+1} \circ A_{t^n} = \partial_t \boldsymbol{\eta}_k \quad \text{on } \Gamma_0. \tag{22}$$

- **Step 2**: Solve the structure sub-problem for the structure displacement $\boldsymbol{\eta}_{k+1}$, driven by the just calculated hydrodynamic force $\mathbf{f}_{s,k+1}$, i.e. $\mathbf{f}_{s,k+1} = J^n\,\widehat{\boldsymbol{\sigma}_{k+1}\boldsymbol{n}}|_{\Gamma^n}$ on Γ^n.

- **Step 3**: Check the stopping criterion, e.g.:

$$\frac{||\boldsymbol{\eta}_{k+1} - \boldsymbol{\eta}_k||}{||\boldsymbol{\eta}_k||} < \epsilon, \tag{23}$$

where ϵ is a given tolerance. If not satisfied, repeat steps 1–3. If satisfied, stop the iterations in k and move to the next step to update the variables at $t = t^{n+1}$.

Update $n+1$: Set $\boldsymbol{u}^{n+1} = \boldsymbol{u}_{k+1}$, $p^{n+1} = p_{k+1}$, and $\boldsymbol{\eta}^{n+1} = \boldsymbol{\eta}_{k+1}$. Solve the ALE problem for displacement $\boldsymbol{d}^{n+1}$ with interface condition $\boldsymbol{d}^{n+1} = \boldsymbol{\eta}^{n+1}$ on Γ_0 and then compute the corresponding fluid domain Ω^{n+1}, ALE map $A_{t^{n+1}}$, and Jacobian J^{n+1}.

It is well known that the convergence properties of the DN algorithm depend heavily on the added-mass effect [23]. In fact, when the structure constitutes a part of the fluid domain boundary, the number of DN iterations required to satisfy the stopping criterion (23) increases as the structure density approaches the fluid density. Moreover, below a certain density ratio ρ_s/ρ_f, which depends on the domain geometry, relaxation is needed for the DN algorithm to converge [63, 64, 23].

The DN algorithm has been shown in [5] to fail for FSI problems with ballon-type structures, i.e., closed structures that contain a certain amount of fluid which must be conserved. This is because in the DN algorithm the coupling conditions are satisfied asynchronously. As a result, the fluid sub-problem uses Dirichlet boundary condition (22) which is based on the velocity of the structure $\partial_t \boldsymbol{\eta}_k$ calculated from the previous sub-iteration. This $\partial_t \boldsymbol{\eta}_k$ may not be consistent with the incompressibility condition (2), giving rise to an ill-posed problem at the semi-descrete level. Because of this limitation, in the next subsection we consider a Robin-Neumann algorithm for the solution of the FSI problem involving closed structures.

3.2. The Robin-Neumann method

At time t^{n+1}, iteration $k+1$, assuming that Ω^n, A_{t^n}, J^n, $\boldsymbol{u}_k$, and $\boldsymbol{\eta}_k$ are known, the following steps are performed:

- **Step 1**: Solve the fluid sub-problem for flow variables of $\boldsymbol{u}_{k+1}$ and p_{k+1} on the fluid domain Ω^n with the following Robin boundary condition:

$$\alpha_f \boldsymbol{u}_{k+1} \circ A_{t^n} - J^n \widehat{\boldsymbol{\sigma}_{k+1}\boldsymbol{n}}|_{\Gamma^n} = \alpha_f \partial_t \boldsymbol{\eta}_k - \mathbf{f}_{s,k} \quad \text{on } \Gamma_0. \tag{24}$$

- **Steps 2**, **3**, and **Update** $n+1$ are as in Sec. 3.1.

Notice that the DN algorithm can be interpreted as a particular case of the RN algorithm for $\alpha_f \to \infty$.

It was shown in [5] that for a suitable choice of parameter α_f the RN method features excellent convergence properties: it always converges without any relaxation and its convergence does not depend on the added-mass effect. In [5] the value of α_f is estimated by considering a simplified structure model. Following [5], we set:

$$\alpha_f = \frac{\rho_s h_s}{\Delta t}. \tag{25}$$

4. The fully discrete problem

We begin by first explaining the time discretization and space discretization of the fluid subproblem, i.e., the subproblem in **Step 1** of the above-mentioned schemes, and then discuss the time and space discretization of the structure sub-problem, i.e., the problem listed in **Step 2** above.

4.1. Time discretization of the fluid problem

Step 1 of both the DN and RN algorithm entails solving fluid problem (7), (8). For the time discretization of problem (7), (8) we consider a second order semi-implicit splitting scheme introduced in [44] for fluid problems in fixed domain. More details about this scheme can be found in [50, 76]. To simplify notation, in this section we omit the subscript $\boldsymbol{x}_0$ in the ALE time derivative term. To advance from time t^n to t^{n+1}, we iterate over k, and for each iteration in k this scheme splits problem (7), (8) into three sub-problems: the first sub-problem deals with the pure advection part (incorporating the fluid and ALE advection simultaneously), the second sub-problem accounts for the incompressibility constraint, and the third sub-problem treats the viscous term. The corresponding updates of the fluid velocity will be denoted by $\boldsymbol{u}_{k+\frac{1}{3}}$, $\boldsymbol{u}_{k+\frac{2}{3}}$, and $\boldsymbol{u}_{k+1}$. They are all defined on Ω^n. In what follows, we will be using the following abbreviated notation: $\boldsymbol{F}^n$ will denote $\boldsymbol{F}(\boldsymbol{u}^n) = \boldsymbol{u}^n \otimes (\boldsymbol{u}^n)^T$. The algorithm is as follows.

- **Step a**: Solve the fluid and ALE advection sub-problem. The inertia term is discretized using the Backward Difference Formula (BDF2 [74]) and the convective term is treated explicitly. The problem reads: given J^{n-1}, $\boldsymbol{u}^{n-1}$, $\boldsymbol{w}^{n-1}$, $\boldsymbol{F}^{n-1}$, and J^n, $\boldsymbol{u}^n$, $\boldsymbol{w}^n$, $\boldsymbol{F}^n$ find the first intermediate velocity field $J^n\boldsymbol{u}_{k+\frac{1}{3}}$ defined on Ω^n such that:

$$\frac{(3J^n\boldsymbol{u}_{k+\frac{1}{3}} - 4J^n\boldsymbol{u}^n + J^{n-1}\boldsymbol{u}^{n-1})}{2\Delta t} = -2J^n\nabla\cdot(\boldsymbol{F}-\boldsymbol{w}\otimes\boldsymbol{u}^T)^n + J^{n-1}\nabla\cdot(\boldsymbol{F}-\boldsymbol{w}\otimes\boldsymbol{u}^T)^{n-1}. \quad (26)$$

- **Step b**: Account for the incompressibility constraint and the associated Lagrange multiplier p_{k+1}. The problem reads: given $J^n\boldsymbol{u}_{k+\frac{1}{3}}$, find p_{k+1} and the second intermediate velocity field $J^n\boldsymbol{u}_{k+\frac{2}{3}}$ defined on Ω^n such that:

$$3\frac{J^n\boldsymbol{u}_{k+\frac{2}{3}} - J^n\boldsymbol{u}_{k+\frac{1}{3}}}{2\Delta t} = -\frac{1}{\rho}\nabla J^n p_{k+1}, \quad (27)$$
$$\nabla\cdot(J^n\boldsymbol{u}_{k+\frac{2}{3}}) = 0.$$

The reason for the 3/2 factor on the left-hand side will be explained below. To solve the above problem, we apply the divergence operator to both sides of eq. (27) to get:

$$\frac{1}{\rho}\Delta J^n p_{k+1} = \frac{3}{2\Delta t}\nabla\cdot(J^n\boldsymbol{u}_{k+\frac{1}{3}}). \quad (28)$$

Problem (28) is supplemented with boundary conditions:

$$\frac{1}{\rho}\frac{\partial J^n p_{k+1}}{\partial \boldsymbol{n}} = -2\boldsymbol{n}\cdot\Big[J^n\boldsymbol{u}_t^n + J^n\big(\nabla\cdot(\boldsymbol{F}-\boldsymbol{w}\otimes\boldsymbol{u}^T)^n - \nu\Delta\boldsymbol{u}^n\big)\Big]$$
$$+\boldsymbol{n}\cdot\Big[J^{n-1}\boldsymbol{u}_t^{n-1} + J^{n-1}\big(\nabla\cdot(\boldsymbol{F}-\boldsymbol{w}\otimes\boldsymbol{u}^T)^{n-1} - \nu\Delta\boldsymbol{u}^{n-1}\big)\Big] \quad \text{on } \partial\Omega_D, \quad (29)$$

$$p_{k+1} = p_N \quad \text{on } \partial\Omega_N, \quad (30)$$

where $\partial\Omega_D$ and $\partial\Omega_N$ are the fixed portions of the boundary where Dirichlet and Neumann data are prescribed, respectively. Furthermore, here $\boldsymbol{u}_t^n = \frac{J^n\boldsymbol{u}^n - J^{n-1}\boldsymbol{u}^{n-1}}{\Delta t}$ is the discrete acceleration Once $J^n p_{k+1}$ has been computed, we plug it into eq. (27) to get $J^n\boldsymbol{u}_{k+\frac{2}{3}}$.

- **Step c**: Solve a Helmholtz problem to treat the viscous term. The problem reads: given $J^n\boldsymbol{u}_{k+\frac{2}{3}}$, find the end-of-step velocity $J^n u_{k+1}$ defined on Ω_0:

$$3\frac{J^n\boldsymbol{u}_{k+1} - J^n\boldsymbol{u}_{k+\frac{2}{3}}}{2\Delta t} = \nu J^n\Delta\boldsymbol{u}_{k+1}. \quad (31)$$

with boundary conditions:

$$\boldsymbol{u}_{k+1} = \boldsymbol{u}_D \quad \text{on } \partial\Omega_D, \quad (32)$$
$$(\nabla\boldsymbol{u}_{k+1})\cdot\boldsymbol{n} = \boldsymbol{0} \quad \text{on } \partial\Omega_N, \quad (33)$$

The 3/2 factor on the left-hand side of both eq. (27) and (31) is there to obtain a second order accurate scheme. That appears clear when eq. (26) is added to eq. (27) and (31):

$$\frac{3J^n\boldsymbol{u}_{k+1} - 3(\cancel{J^n\boldsymbol{u}_{k+\frac{2}{3}}} - \cancel{J^n\boldsymbol{u}_{k+\frac{2}{3}}} + \cancel{J^n\boldsymbol{u}_{k+\frac{1}{3}}} - \cancel{J^n\boldsymbol{u}_{k+\frac{1}{3}}}) - 4J^n\boldsymbol{u}^n + J^{n-1}\boldsymbol{u}^{n-1}}{2\Delta t}$$
$$-\nu J^n\Delta\boldsymbol{u}_{k+1} + \frac{1}{\rho}\nabla J^n p_{k+1} = -2J^n\nabla\cdot(\boldsymbol{F}-\boldsymbol{w}\otimes\boldsymbol{u}^T)^n + J^{n-1}\nabla\cdot(\boldsymbol{F}-\boldsymbol{w}\otimes\boldsymbol{u}^T)^{n-1}.$$

Moreover, notice that velocity $\boldsymbol{u}_{k+1}$ and pressure p_{k+1} satisfy boundary conditions (3),(4), i.e. $\boldsymbol{u}_{k+1} = \boldsymbol{u}_D$ on $\partial\Omega_D\times(0,T)$ and $\boldsymbol{\sigma}_{k+1}\boldsymbol{n} = -p_N\boldsymbol{n}$ on $\partial\Omega_N\times(0,T)$.

This scheme is referred to as semi-implicit since the convective term is treated explicitly, while the viscous and pressure terms are treated implicitly.

4.2. Space discretization of the fluid problem

For the space discretization of problem (7), (8) we consider a high order Discontinuous Galerkin (DG) method [54]. The use of DG methods for incompressible, viscous fluids is motivated by applications in which some of the state variables may have a jump. This includes, for example, a jump in the pressure, which occurs in blood flow problems with an immersed structure, such as a stent-graft used in the treatment of Aortic Abdominal Aneurysm, discussed in Sec. 5.5, or the motion of closed, immersed structures, discussed in Sec. 5.4, which occurs in blood flow applications when modeling the interaction between red blood cells and blood flow.

For simplicity, in this section we present the details for a 2D problem discretized in space with triangular meshes. Extensions to 3D, while computationally demanding, are conceptually straightforward as we show in Secs. 5.1 and 5.5, see also [54].

Let $\mathcal{T}_h$ be a conformal and quasi-uniform partition of Ω. Let x and y be the space coordinates of the 2D computational domain and let E be the generic element of $\mathcal{T}_h$. Let r and s be the space coordinates for the reference triangular element $\hat{E}$, which is the standard isosceles right triangle that every element $\hat{E}$ of $\mathcal{T}_h$ can be mapped to. The unknowns of the problem can be written locally as linear combinations of modal basis functions or nodal basis functions. For example, a generic function $u(x, y)$ defined on a local triangular element E can be written as:

$$u(x,y) = \sum_{i=1}^{N} \hat{u}_i \Phi_i(x,y) = \sum_{j=1}^{N} u_j l_j(x,y), \quad (x,y) \in E, \tag{34}$$

where $\hat{u}_i$ are the local expansion coefficients associated with orthonormal modal basis $\{\Phi_i(x,y)\}_{i=1}^N$, while u_j are the local expansion coefficients associated with nodal basis $\{l_j(x,y)\}_{j=1}^N$. Each $\{l_j(x,y)\}$ coincides with the value of $u(x,y)$ at the grid point $(x,y)_j$ on triangular element E. For simplicity, eq. (34) assumes that the number of nodes and the number of modes are both equal to N. We will stick to this assumption for the rest of this section. In 2D, if we are using (modal or nodal) polynomials of n-th degree we have $N = (n+1)(n+2)/2$. In this paper, we will consider approximations with nodal basis functions (Lagrangian polynomials).

There are two main difficulties associated with nodal bases. Firstly, it is nontrivial to build high order nodal bases for triangular elements. In fact, one needs to find a set of interpolation points that satisfy two requirements: the associated basis functions have to remain linearly independent when the order increases and the condition number of the associated system matrix has to remain relatively small. Secondly, those interpolation points are not necessarily good quadrature points for the approximation of integrals. To face the first issue, we use the so-called Fekete points shown in Fig. 2(b) for $n = 4$ on triangular elements. For details on the properties of these points we refer to [54]. The second issue is addressed by expressing nodal basis functions in terms of modal basis functions in order to simplify numerical integration [54].

More precisely, we begin by considering a set of orthonormal polynomial modes defined on the reference triangle $\hat{E}$, reported in [46, 33, 50]:

$$\widehat{\Phi}_i(r,s) = \sqrt{2} P_k^{0,0}\left(2\frac{1+r}{1-s} - 1\right) P_l^{(2k+1,0)}(s)(1-s)^k, \quad (r,s) \in \hat{E}.$$

Here, subscript i stands for the i-th mode of the basis functions, and $i = (N+1)k + l + 1 - \frac{k}{2}(k-1)$, with $k, l \geq 0$ and $k + l \leq N$, $P_k^{(\alpha,\beta)}(s)$ is a Jacobi polynomial of order k where $\alpha, \beta > -1$ define the power of the weight $(1-s)^\alpha (1+s)^\beta$. Jacobi polynomials are a family of polynomial solutions to the singular Sturm-Liouville problem. Fig. 2(a) shows all the modes ($N = 15$) of the 4^{th} order ($n = 4$) modal basis functions on the reference triangular element $\hat{E}$. We will use a "hat" for all the functions defined on the reference element $\hat{E}$, e.g., $\widehat{\Phi}_i(r,s)$ defined on $\hat{E}$ is the corresponding function to $\Phi_i(x,y)$ defined on E.

To write the nodal basis functions on $\hat{E}$ in terms of the modal basis functions described above, we introduce the generalized Vandermonde matrix V [50, 54] with entries:

$$V_{ij} = \widehat{\Phi}_j(r,s)_i, \quad i,j = 1,\ldots,N.$$

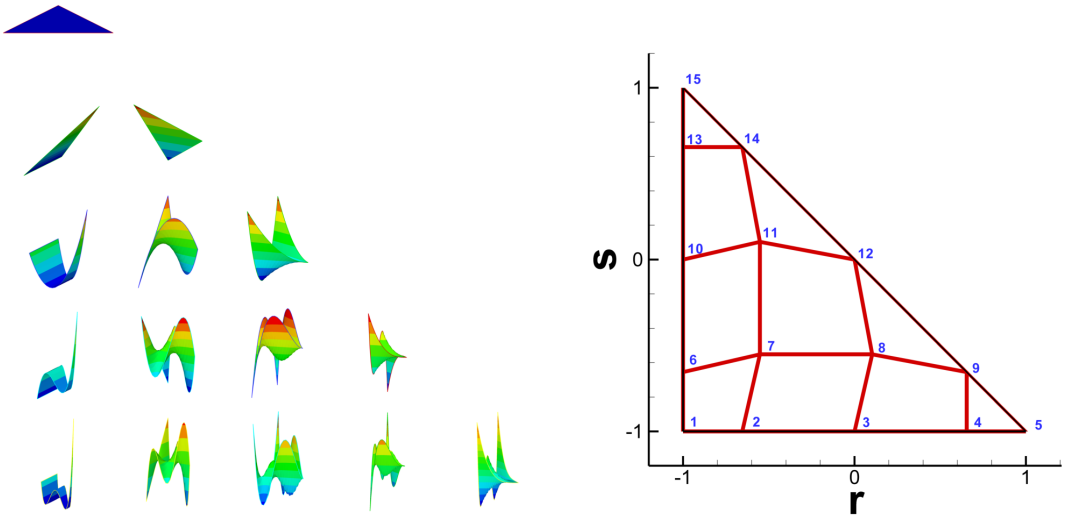

Figure 2: (a) Modal basis functions $\mathbf{\Phi}_j$, $j = 1, \ldots, 15$, defined on the standard isosceles right triangle $\hat{E}$ for $n = 4$ and (b) corresponding Fekete points in $\hat{E}$.

Let $\widehat{\boldsymbol{l}} = [\widehat{l}_1, \widehat{l}_2, ..., \widehat{l}_N]^T$ and $\widehat{\mathbf{\Phi}} = [\widehat{\Phi}_1, \widehat{\Phi}_2, ..., \widehat{\Phi}_N]^T$ denote the nodal and modal basis functions on reference triangle $\hat{E}$. We have:

$$\widehat{\boldsymbol{l}} = (V^T)^{-1}\widehat{\mathbf{\Phi}},$$

that is, nodal basis $\widehat{l}_i$ on reference triangle $\hat{E}$ can be expressed as:

$$\widehat{l}_i = \sum_{k=1}^{N} (V^T)^{-1}_{ik} \widehat{\Phi}_k.$$

The mass matrix defined on reference triangle $\hat{E}$ is given by:

$$\begin{aligned} M_{ij} &= \int_{\hat{E}} \widehat{l}_i \widehat{l}_j \; drds = \int_{\hat{E}} \Big(\sum_{k=1}^{N} (V^T)^{-1}_{ik} \widehat{\Phi}_k \sum_{l=1}^{N} (V^T)^{-1}_{jl} \widehat{\Phi}_l \Big) \; drds \\ &= \sum_{k=1}^{N} \sum_{l=1}^{N} (V^T)^{-1}_{ik} (V^T)^{-1}_{jl} \underbrace{\int_{\hat{E}} \widehat{\Phi}_k \widehat{\Phi}_l \; drds}_{\delta_{kl}} = \sum_{k=1}^{N} (V^T)^{-1}_{ik} (V^T)^{-1}_{jk} = \sum_{k=1}^{N} (V^T)^{-1}_{ik} (V)^{-1}_{kj} = (VV^T)^{-1}_{ij}, \end{aligned}$$

with $i, j = 1, \ldots, N$. The mass matrix M_E for a generic element E is given by:

$$M_{Eij} = \int_E l_i l_j \; dxdy = J_E M_{ij},$$

where $J_E = \det \left| \frac{\partial(x,y)}{\partial(r,s)} \right|$ is the Jacobian of the affine transformation that maps E into $\hat{E}$.

Next we define the local matrix L_E associated with the divergence operator by:

$$L_E = \left[L_{E_x}, L_{E_y} \right]^T,$$

where

$$(L_{E_x})_{i,j} = \int_E l_i \frac{\partial l_j}{\partial x} dxdy, \quad (L_{E_y})_{i,j} = \int_E l_i \frac{\partial l_j}{\partial y} dxdy, \; i, j = 1, \ldots, N.$$

The x and y components L_{E_x} and L_{E_y} correspond to the x and y derivatives in the gradient operator. Note that L_E is an $N \times 2N$ matrix. It is convenient to write L_E in terms of the (r, s) coordinates defined on the reference triangle $\hat{E}$ as follows:

$$
\begin{aligned}
(L_{E_x})_{i,j} &= \int_{\hat{E}} \widehat{l}_i \left[\frac{\partial \widehat{l}_j}{\partial r} \frac{\partial r}{\partial x} + \frac{\partial \widehat{l}_j}{\partial s} \frac{\partial s}{\partial x} \right] J_E dr ds \\
&= \int_{\hat{E}} \widehat{l}_i \sum_{k=1}^{N} \left[\frac{\partial \widehat{l}_j}{\partial r}\Big|_{(r,s)_k} \frac{\partial r}{\partial x}\Big|_{(r,s)_k} + \frac{\partial \widehat{l}_j}{\partial s}\Big|_{(r,s)_k} \frac{\partial s}{\partial x}\Big|_{(r,s)_k} \right] \widehat{l}_k J_E dr ds. \qquad (35)
\end{aligned}
$$

By using the following relationships [50]:

$$
\frac{\partial r}{\partial x} = \frac{1}{J_E}\frac{\partial y}{\partial s}, \frac{\partial r}{\partial y} = -\frac{1}{J_E}\frac{\partial x}{\partial s}, \frac{\partial s}{\partial x} = -\frac{1}{J_E}\frac{\partial y}{\partial r}, \frac{\partial s}{\partial y} = \frac{1}{J_E}\frac{\partial x}{\partial r},
$$

we write (35) as

$$
(L_{E_x})_{i,j} = \int_{\hat{E}} \widehat{l}_i \sum_{k=1}^{N} \left[\frac{\partial \widehat{l}_j}{\partial r}\Big|_{(r,s)_s} \frac{\partial y}{\partial s}\Big|_{(r,s)_k} - \frac{\partial \widehat{l}_j}{\partial s}\Big|_{(r,s)_k} \frac{\partial y}{\partial r}\Big|_{(r,s)_k} \right] \widehat{l}_k dr ds.
$$

Similarly,

$$
(L_{E_y})_{i,j} = \int_{\hat{E}} \widehat{l}_i \sum_{k=1}^{N} \left[-\frac{\partial \widehat{l}_j}{\partial r}\Big|_{(r,s)_s} \frac{\partial x}{\partial s}\Big|_{(r,s)_k} + \frac{\partial \widehat{l}_j}{\partial s}\Big|_{(r,s)_k} \frac{\partial x}{\partial r}\Big|_{(r,s)_k} \right] \widehat{l}_k dr ds,
$$

$i, j = 1, \ldots N$.

We are now in a position to write the matrix form of the three subproblems discussed in Sec. 4.1. We use boldface characters to denote the arrays of nodal values for each variable.

- **Step a**: The full discretization of problem (26) yields the system

$$
M_E \frac{3J^n \mathbf{u}_{k+\frac{1}{3}} - 4J^n \mathbf{u}^n + J^{n-1}\mathbf{u}^{n-1}}{2\Delta t} = -2J^n L_E \cdot (\mathbf{F} - \mathbf{w} \otimes \mathbf{u}^T)^n + J^{n-1} L_E \cdot (\mathbf{F} - \mathbf{w} \otimes \mathbf{u}^T)^{n-1} + \mathbf{b}_1.
$$

  Here, the entries of vector $\mathbf{b}_1$ are given by:

$$
\begin{aligned}
\mathbf{b}_{1,j} = \int_{\partial E} \boldsymbol{n} \cdot [&- 2J^n \big((\boldsymbol{F} - \boldsymbol{w} \otimes \boldsymbol{u}^T) - (\boldsymbol{F} - \boldsymbol{w} \otimes \boldsymbol{u}^T)^* \big)^n \\
&+ J^{n-1} \big((\boldsymbol{F} - \boldsymbol{w} \otimes \boldsymbol{u}^T) - (\boldsymbol{F} - \boldsymbol{w} \otimes \boldsymbol{u}^T)^* \big)^{n-1} \Big] l_j \, d\xi, \quad j = 1, \ldots, N.
\end{aligned}
$$

  where $d\xi$ denotes integration along the boundary ∂E, and $(\boldsymbol{F} - \boldsymbol{w} \otimes \boldsymbol{u}^T)^*$ denotes the local Lax-Friedrichs flux:

$$
(\boldsymbol{F} - \boldsymbol{w} \otimes \boldsymbol{u}^T)^* = \frac{(\boldsymbol{F} - \boldsymbol{w} \otimes \boldsymbol{u}^T)^+ + (\boldsymbol{F} - \boldsymbol{w} \otimes \boldsymbol{u}^T)^- + \tau(\boldsymbol{u}^+ - \boldsymbol{u}^-)}{2}.
$$

  As usual, superscripts $^+$ and $^-$ indicate exterior and interior values for element E, and coefficient τ is the local maximum value of the directional flux Jacobian [50]. Recall that L_E is the discretized divergence operator and $\mathbf{b}_1$ comes from the boundary terms from integration by parts.

- **Step b**: Following [28], we introduce an auxiliary variable $\boldsymbol{q}$ to write eq. (28) as an equivalent first order system:

$$
\frac{J^n}{\rho} \nabla p_{k+1} = \boldsymbol{q}, \qquad (36)
$$

$$
\nabla \cdot \boldsymbol{q} = \frac{3}{2\Delta t} \nabla \cdot (J^n \boldsymbol{u}_{k+\frac{1}{3}}), \qquad (37)
$$

with $\boldsymbol{q} = (q_x, q_y)$. On each triangle E, we approximate (p_{k+1}, q_x, q_y) with the N^{th} order nodal basis $\{l_j\}_{j=1}^N$ constructed on that triangle. Let us introduce the following interior penalty fluxes:

$$p^* = \frac{p_{k+1}^+ + p_{k+1}^-}{2}, \quad \boldsymbol{q}^* = (q_x^*,\ q_y^*) = \frac{J^n}{\rho}\Big(\frac{\nabla(p_{k+1})^+ + \nabla(p_{k+1})^-}{2} - \tau\big[\boldsymbol{n}^-(p_{k+1})^- + \boldsymbol{n}^+(p_{k+1})^+\big]\Big),$$

where τ is the penalty parameter. We refer to [80] for how to set the value of τ. The subscript $k+1$ is omitted for $\boldsymbol{q}, \boldsymbol{q}^*, p^*$ to simplify notation. The interior penalty flux $\boldsymbol{q}^*$ serves the role to eliminate large jumps in p_{k+1} between the adjacent elements when the pressure is continuous. To define $\boldsymbol{n}^+$ and $\boldsymbol{n}^-$, we note that adjacent elements do not necessarily have aligned edges as a result of the ALE mapping. If the edges are aligned, $\boldsymbol{n}^- = -\boldsymbol{n}^+$. If the edges are not aligned, $\boldsymbol{n}^+$ is the outward normal for element E and $\boldsymbol{n}^-$ is the outward normal to the corresponding edge for the adjacent element. See Fig. 3.

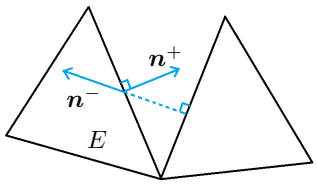

Figure 3: Neighboring elements with edges that are not aligned: outward normal $\boldsymbol{n}^+$ for element E and outward normal $\boldsymbol{n}^-$ to the corresponding edge for the adjacent element. The gap between the edges is exaggerated for visualization purposes. In practice, we keep the gaps between the neighboring elements at the minimum by using interior penalty. See Sec. 4.5.

To write the discretized problem, we will again be using $\mathbf{p}$ and $\mathbf{q}$ to denote the vectors corresponding to the nodal values of p and $\boldsymbol{q}$. We define vector $\mathbf{b}_{2,x}$ and $\mathbf{b}_{2,y}$ on E:

$$(\mathbf{b}_{2,x})_j = \int_{\partial E} n_x\big(p_{k+1} - p^*\big) l_j d\xi, (\mathbf{b}_{2,y})_j = \int_{\partial E} n_y\big(p_{k+1} - p^*\big) l_j d\xi, \quad j = 1, \ldots, N,$$

where $\boldsymbol{n} = (n_x, n_y)$ is the outward normal to ∂E. Notice that for a given element $\boldsymbol{n}$ coincides with $\boldsymbol{n}^+$ introduced above. The matrix form of eq. (36) on element E is given by:

$$\frac{J^n}{\rho}\Big(L_{E_x}\mathbf{p}_{k+1} - \mathbf{b}_{2,x}\Big) = M_E\ \mathbf{q}_x, \frac{J^n}{\rho}\Big(L_{E_y}\mathbf{p}_{k+1} - \mathbf{b}_{2,y}\Big) = M_E\ \mathbf{q}_y.$$

The matrix form of (37) on element E is:

$$L_{E_x}\mathbf{q}_x + L_{E_y}\mathbf{q}_y = \frac{3}{2\Delta t} L_E \cdot (J^n \mathbf{u}_{k+\frac{1}{3}}) + \mathbf{b}_3,$$

with $(\mathbf{b}_3)_j = \int_{\partial E} \boldsymbol{n} \cdot (q_x - q_x^*,\ q_y - q_y^*) l_j\ d\xi$, for $j = 1, \ldots, N$.

- **Step c**: We follow a procedure similar to Step b. Let $\boldsymbol{u} = (u_x, u_y)$. We introduce auxiliary variables $\boldsymbol{g}_x = (g_{x,x}, g_{x,y})$ and $\boldsymbol{g}_y = (g_{y,x}, g_{y,y})$ to write eq. (31) as an equivalent system of first order equations:

$$\nabla u_{x,k+1} = \boldsymbol{g}_x, \quad \nabla u_{y,k+1} = \boldsymbol{g}_y, \tag{38}$$

$$3\frac{J^n u_{x,k+1} - J^n u_{x,k+\frac{2}{3}}}{2\Delta t} = \nu J^n \nabla \cdot \boldsymbol{g}_x, \quad 3\frac{J^n u_{y,k+1} - J^n u_{y,k+\frac{2}{3}}}{2\Delta t} = \nu J^n \nabla \cdot \boldsymbol{g}_y. \tag{39}$$

Let us introduce also the following interior penalty fluxes:

$$u_x^* = \frac{(u_{x,k+1})^+ + (u_{x,k+1})^-}{2}, \quad u_y^* = \frac{(u_{y,k+1})^+ + (u_{y,k+1})^-}{2},$$
$$\boldsymbol{g}_x^* = (g_{x,x}^*, g_{x,y}^*) = \frac{\nabla(u_{x,k+1})^+ + \nabla(u_{x,k+1})^-}{2} - \tau\big[\boldsymbol{n}^-(u_{x,k+1})^- + \boldsymbol{n}^+(u_{x,k+1})^+\big],$$
$$\boldsymbol{g}_y^* = (g_{y,x}^*, g_{y,y}^*) = \frac{\nabla(u_{y,k+1})^+ + \nabla(u_{y,k+1})^-}{2} - \tau\big[\boldsymbol{n}^-(u_{y,k+1})^- + \boldsymbol{n}^+(u_{y,k+1})^+\big],$$

where τ is the penalty parameter [80]. The matrix form of eq. (31) is given by:

$$L_{E_x}\mathbf{u}_{x,k+1} = M_E\ \mathbf{g}_{x,x} + \mathbf{b}_{4,x,x}, \quad L_{E_y}\mathbf{u}_{x,k+1} = M_E\ \mathbf{g}_{x,y} + \mathbf{b}_{4,x,y},$$
$$L_{E_x}\mathbf{u}_{y,k+1} = M_E\ \mathbf{g}_{y,x} + \mathbf{b}_{4,y,x}, \quad L_{E_y}\mathbf{u}_{y,k+1} = M_E\ \mathbf{g}_{y,y} + \mathbf{b}_{4,y,y},$$
$$\frac{3}{2\Delta t}M_E(J^n\mathbf{u}_{x,k+1} - J^n\mathbf{u}_{x,k+\frac{2}{3}}) = \nu J^n\Big[L_{E_x}\mathbf{g}_{x,x} + L_{E_y}\mathbf{g}_{x,y} - \mathbf{b}_{5,x}\Big],$$
$$\frac{3}{2\Delta t}M_E(J^n\mathbf{u}_{y,k+1} - J^n\mathbf{u}_{y,k+\frac{2}{3}}) = \nu J^n\Big[L_{E_x}\mathbf{g}_{y,x} + L_{E_y}\mathbf{g}_{y,y} - \mathbf{b}_{5,y}\Big],$$

where vectors $\mathbf{b}_{4,x}$, $\mathbf{b}_{4,y}$ and $\mathbf{b}_5$ on each element E are defined as follows:

$$(\mathbf{b}_{4,x,x})_j = \int_{\partial E} n_x\big(u_{x,k+1} - u_x^*\big)l_j\ d\xi, \quad (\mathbf{b}_{4,x,y})_j = \int_{\partial E} n_y\big(u_{x,k+1} - u_x^*\big)l_j\ d\xi,$$
$$(\mathbf{b}_{4,y,x})_j = \int_{\partial E} n_x\big(u_{y,k+1} - u_y^*\big)l_j\ d\xi, \quad (\mathbf{b}_{4,y,y})_j = \int_{\partial E} n_y\big(u_{y,k+1} - u_y^*\big)l_j\ d\xi,$$
$$(\mathbf{b}_{5,x})_j = \int_{\partial E} \boldsymbol{n}\cdot(g_{x,x} - g_{x,x}^*,\ g_{x,y} - g_{x,y}^*)l_j\ d\xi,$$
$$(\mathbf{b}_{5,y})_j = \int_{\partial E} \boldsymbol{n}\cdot(g_{y,x} - g_{y,x}^*,\ g_{y,y} - g_{y,y}^*)l_j\ d\xi, \quad j = 1,\dots,N.$$

4.3. Time discretization of the structure problem

At the Step 2 of both the DN and RN algorithm we have to solve the structure problem. In this section we focus on the time discretization of problem (13) and in the next section we describe its space discretization. As for problem (12),(17), its full discretization is trivial since it does not contain spatial derivatives.

In order to devise a time splitting scheme, we introduce variables:

$$U = \rho_s h_s\frac{\partial\eta_y}{\partial t} - \gamma\frac{\partial^2\eta_y}{\partial x^2} \quad \text{and} \quad W = \frac{\partial^2\eta_y}{\partial x^2}.$$

Problem (13) can be equivalently written as the following first-order system in time:

$$\rho_s h_s\frac{\partial\eta_y}{\partial t} = U + \gamma W \quad \text{in } \Gamma_0\times(0,T),$$
$$\frac{\partial U}{\partial t} = kGh_sW - \frac{Eh_s}{(1-\nu^2)}\frac{\eta_y}{R_0^2} + f_{s,y} \quad \text{in } \Gamma_0\times(0,T),$$

with initial conditions:

$$\eta_y = 0,\ \frac{\partial\eta_y}{\partial t} = 0, U = \rho_s h_s\frac{\partial\eta_y}{\partial t} - \gamma W = 0, \quad \text{in } \Gamma_0\times\{0\}.$$

For the time discretization of the above system we use the forward Euler scheme. The time discrete problem

reads: given η_y^n, U^n, W^n and $f_{s,k+1}$, find $\eta_{y,k+1}$, U_{k+1} and W_{k+1} such that

$$\frac{U_{k+1}-U^n}{\Delta t} = kGh_sW^n - \frac{Eh_s}{1-\nu^2}\frac{\eta_y^n}{R_0^2} + f_{s,k+1}, \tag{40}$$

$$\rho_s h_s \frac{\eta_{y,k+1}-\eta_y^n}{\Delta t} = U_{k+1} + \gamma W^n, \tag{41}$$

$$W_{k+1} = \frac{\partial^2 \eta_{y,k+1}}{\partial x^2}. \tag{42}$$

We remind the reader that $f_{s,k+1}$ is the force coming from the fluid normal stress, which in this scheme comes from the just calculated fluid subproblem in **Step 1**.

4.4. Space discretization of the structure problem

We use the nodal DG method for the space discretization of system (40)-(42). We recall that system (40)-(42) describes a 1D structure that lies on a part of a 2D fluid domain boundary. We consider matching fluid and structure meshes, i.e. the structure mesh will be made up of the edges of the fluid elements that lie on Γ_0. Therefore, to construct the structure nodal basis functions $\{l_j^s(x)\}_{j=1}^N$ we use the interpolation points on the sides of the fluid mesh triangles that lie on Γ_0. Normalized Legendre polynomials [28] are used to built the Vandermonde matrix. We follow a similar procedure to the one described in Sec. 4.2 to construct the local mass matrix M_E^s and differential matrix L_E^s.

The martix forms of eq. (41) and eq. (40) are given by:

$$\rho_s h_s M_E^s\ \boldsymbol{\eta}_{y,k+1} = \rho_s h_s M_E^s\ \boldsymbol{\eta}_y^n + \Delta t M_E^s\Big(\mathbf{U}_{k+1} + \gamma \mathbf{W}^n\Big),$$

$$M_E^s \mathbf{U}_{k+1} = M_E^s \mathbf{U}^n + \Delta t M_E^s\Big(kGh_s\mathbf{W}^n - \frac{Eh_s}{1-\nu^2}\frac{\boldsymbol{\eta}_y^n}{R_0^2} + \mathbf{f}_{s,k+1}\Big),$$

where the vectors $\boldsymbol{\eta}_y$, $\mathbf{W}$, $\mathbf{U}$ denote the nodal values of the state variables η_y, W, and U.

As for eq. (42), we introduce an intermediate variable q_{k+1} to write it as an equivalent system of first order differential equations in space:

$$q_{k+1} = \frac{\partial \eta_{y,k+1}}{\partial x},$$

$$W_{k+1} = \frac{\partial q_{k+1}}{\partial x}.$$

The matrix form of the above system is:

$$M_E^s\ \mathbf{q}_{k+1} = L_E^s\ \boldsymbol{\eta}_{y,k+1} - \mathbf{b}_6,$$

$$M_E^s\ \mathbf{W}_{k+1} = L_E^s\ \mathbf{q}_{k+1} - \mathbf{b}_7,$$

where local vectors $\mathbf{b}_6$ and $\mathbf{b}_7$ are given by:

$$(\mathbf{b}_6)_j = \int_{\partial E\cap\Gamma_0} \boldsymbol{n}\cdot(\eta_{y,k+1}-\eta_y^*)l_j^s d\xi, \quad (\mathbf{b}_7)_j = \int_{\partial E\cap\Gamma_0} \boldsymbol{n}\cdot(q_{k+1}-q^*)l_j^s d\xi, \quad j=1,\dots,N.$$

Here, we take the flux pairs $q^* = q_{k+1}^-$ and $\eta_y^* = \eta_{y,k+1}^+$, or $q^* = q_{k+1}^+$ and $\eta_y^* = \eta_{y,k+1}^-$, to guarantee stability. More details and analysis of this choice can be found in [84].

4.5. Space discretization of the ALE problem

We conclude this section by describing the space discretization of the ALE problem that needs to be solved at the end of both the DN and RN algorithms. Since we have already implemented the DG method to solve a parabolic problem for the fluid, it is computationally inexpensive to then use the DG method with interior penalty to also solve the corresponding elliptic problem for the Laplace's equation [2, 1, 80], which needs to be solved to update the mesh.

Following what we have done in Secs. 4.2 and 4.4, we write eq. (9) as a system of two first order equations for each component of displacement vector $\boldsymbol{d} = (d_x, d_y)$:

$$\nabla d_x = \boldsymbol{h}_x, \quad \nabla d_y = \boldsymbol{h}_y, \quad \nabla \cdot \boldsymbol{h}_x = 0, \quad \nabla \cdot \boldsymbol{h}_y = 0 \quad \text{in} \quad \Omega_0, \tag{43}$$

where $\boldsymbol{h}_x = (h_{x,x}, h_{x,y})$ and $\boldsymbol{h}_y = (h_{y,x}, h_{y,y})$.

To keep the gaps between the neighboring elements at the minimum, we introduce the following interior penalty flux:

$$\begin{aligned} d_x^* &= \frac{d_x^+ + d_x^-}{2}, \quad \boldsymbol{h}_x^* = [h_{x,x}^*,\ h_{x,y}^*]^T = \frac{\nabla d_x^+ + \nabla d_x^-}{2} - \tau[\boldsymbol{n}^- d_x^- + \boldsymbol{n}^+ d_x^+], \\ d_y^* &= \frac{d_y^+ + d_y^-}{2}, \quad \boldsymbol{h}_y^* = [h_{y,x}^*,\ h_{y,y}^*]^T = \frac{\nabla d_y^+ + \nabla d_y^-}{2} - \tau[\boldsymbol{n}^- d_y^- + \boldsymbol{n}^+ d_y^+], \end{aligned}$$

where parameter τ is the penalty parameter [80]. After writing this system in weak form, integrating by parts, and discretizing it, we obtain the following matrix form of the discretized system (43), defined on each triangle:

$$\begin{aligned} &L_{E_x}\ \mathbf{d_x} = M_E\ \mathbf{h}_{x,x} + \mathbf{b}_{8,x,x}, \quad L_{Ey}\ \mathbf{d_x} = M_E\ \mathbf{h}_{x,y} + \mathbf{b}_{8,x,y}, \\ &L_{E_x}\ \mathbf{d_y} = M_E\ \mathbf{h}_{y,x} + \mathbf{b}_{8,y,x}, \quad L_{Ey}\ \mathbf{d_y} = M_E\ \mathbf{h}_{y,y} + \mathbf{b}_{8,y,y}, \\ &L_{E_x}\ \mathbf{h}_{x,x} + L_{E_y}\ \mathbf{h}_{x,y} = \mathbf{b}_{9,x}, \quad L_{E_x}\ \mathbf{h}_{y,x} + L_{E_y}\ \mathbf{h}_{y,y} = \mathbf{b}_{9,y}, \end{aligned}$$

where:

$$\begin{aligned} (\mathbf{b}_{8,x,x})_j &= \int_{\partial E} n_x(d_x - d_x^*) l_j dx dy, \quad (\mathbf{b}_{8,x,y})_j = \int_{\partial E} n_y(d_x - d_x^*) l_j\ d\xi, \\ (\mathbf{b}_{8,y,x})_j &= \int_{\partial E} n_x(d_y - d_y^*) l_j dx dy, \quad (\mathbf{b}_{8,y,y})_j = \int_{\partial E} n_y(d_y - d_y^*) l_j\ d\xi, \\ (\mathbf{b}_{9,x})_j &= \int_{\partial E} \boldsymbol{n} \cdot (q_{x,x} - q_{x,x}^*,\ q_{x,y} - q_{x,y}^*) l_j\ d\xi, \\ (\mathbf{b}_{9,y})_j &= \int_{\partial E} \boldsymbol{n} \cdot (q_{y,x} - q_{y,x}^*,\ q_{y,y} - q_{y,y}^*) l_j\ d\xi, \quad j = 1, \ldots, N. \end{aligned}$$

4.6. The implementation of the Robin-Neumann algorithm for immersed structures

The time-splitting algorithm for the fluid sub-problem, described in Sec. 4.1, makes the implementation of the Robin-Neumann algorithm tricky, in particular for immersed structures. In fact, when the structure is immersed Robin boundary condition (24) becomes:

$$\alpha_f \boldsymbol{u}_{k+1} \circ A_{t^n} - J^n\ [\![\widehat{\boldsymbol{\sigma}_{k+1}\boldsymbol{n}}]\!]|_{\Gamma^n} = \alpha_f \partial_t \boldsymbol{\eta}_k - \mathbf{f}_{s,k} \quad \text{on } \Gamma_0. \tag{44}$$

The main difficulty comes from calculating the jump in the normal stress, appearing in the second term on the left hand-side of (44). Another difficulty is related to the fact that the splitting algorithm in Sec. 4.2 requires boundary conditions for the velocity sub-problem (31) and for the pressure sub-problem (28).

To get around this difficulty we rewrite the Robin boundary condition (44) as follows. First, the Cauchy stress tensor is explicitly written as shown below:

$$\alpha_f \boldsymbol{u}_{k+1} \circ A_{t^n} - J^n\ [\![-\widehat{p_{k+1}\mathbf{I}\boldsymbol{n}} + 2\nu\rho\mathbf{D}(\widehat{\boldsymbol{u}_{k+1}})\boldsymbol{n}]\!]|_{\Gamma^n} = \alpha_f \partial_t \boldsymbol{\eta}_k - \mathbf{f}_{s,k} \quad \text{on } \Gamma_0. \tag{45}$$

Notice that $\nu\rho = \mu$ is the dynamics viscosity of the fluid. Next, equation (45) is separated into two parts: one will be used as a boundary condition for the pressure sub-problem (28) along Γ_0, and the other will be used in the velocity sub-problem (31) along Γ_0. More precisely, we rewrite (45) as follows:

$$J^n \, [\![\widehat{p_{k+1}\mathbf{I}\boldsymbol{n}}]\!]|_{\Gamma^n} \cdot \boldsymbol{n} = \Big(\alpha_f \partial_t \boldsymbol{\eta}_k - \mathbf{f}_{s,k} - \alpha_f \boldsymbol{u}_k \circ A_{t^n} + J^n \, [\![2\mu \widehat{\mathbf{D}(\boldsymbol{u}_k)\boldsymbol{n}}]\!]|_{\Gamma^n}\Big) \cdot \boldsymbol{n}, \tag{46}$$

$$\alpha_f \boldsymbol{u}_{k+1} \circ A_{t^n} = \alpha_f \partial_t \boldsymbol{\eta}_k - \mathbf{f}_{s,k} + J^n \, [\![-\widehat{p_{k+1}\mathbf{I}\boldsymbol{n}} + 2\mu \widehat{\mathbf{D}(\boldsymbol{u}_k)\boldsymbol{n}}]\!]|_{\Gamma^n}, \quad \text{on } \Gamma_0. \tag{47}$$

Then, we introduce $\widehat{p}^{+}_{k+1}|_{\Gamma_n}$ and $\widehat{p}^{-}_{k}|_{\Gamma_n}$ to denote the pressure on either side of the interface Γ^n at time t^{n+1}, at iterations $k+1$ and k respectively. The superscripts $+$ and $-$ denote the pressures on the "right" and "left" sides of the boundary Γ^n, where "right" and "left" are determined by the orientation of the normal $\boldsymbol{n}$ to Γ^n. Notice that the exterior pressure is taken at iteration k which is known. Then, we have:

$$\widehat{p}^{-}_{k+1}|_{\Gamma^n} = \widehat{p}^{+}_{k}|_{\Gamma^n} + [\![\widehat{p}_{k+1}]\!]|_{\Gamma^n}.$$

With this strategy, the Robin boundary condition (44) is converted into boundary conditions for the pressure sub-problem (28):

$$J^n \widehat{p}_{k+1}|_{\Gamma^n} = J^n \widehat{p}^{+}_{k}|_{\Gamma^n} + (\alpha_f \partial_t \boldsymbol{\eta}_k - \mathbf{f}_{s,k}) \cdot \boldsymbol{n} - \alpha_f \boldsymbol{u}_k \circ A_{t^n} \cdot \boldsymbol{n} + J^n 2\mu [\![\widehat{\mathbf{D}(\boldsymbol{u}_k)\boldsymbol{n}}]\!]|_{\Gamma^n} \cdot \boldsymbol{n} \quad \text{on } \Gamma_0, \tag{48}$$

and the boundary condition for the velocity sub-problem (31):

$$\alpha_f \boldsymbol{u}_{k+1} \circ A_{t^n} = \alpha_f \partial_t \boldsymbol{\eta}_k - \mathbf{f}_{s,k} + J^n [\![-\widehat{p_{k+1}\mathbf{I}\boldsymbol{n}} + 2\mu \widehat{\mathbf{D}(\boldsymbol{u}_k)\boldsymbol{n}}]\!]|_{\Gamma^n} \qquad \text{on } \Gamma_0. \tag{49}$$

With this approach we partitioned the Robin boundary condition involving the fluid velocity and normal stress implicitly on the left hand-side of (45), into two boundary conditions of Dirichlet type, but still involving the fluid velocity and pressure (the dominant component of normal stress) implicitly on the left hand-sides of conditions (49) and (48).

Our numerical simulations presented in Sec. 5.4 show that this approach provides a good approximation of the solution for the corresponding FSI problem with an immersed closed structure, i.e., a "bubble" problem.

5. Numerical results

5.1. Benchmark test 1: 2D and 3D simulations of flow past a cylinder

We begin by considering a classical benchmark problem in fluid dynamics which consists of studying the flow of an incompressible, viscous fluid past a circular cylinder [79, 53]. We report the results of our 2D and 3D simulations, and compare them with results in the literature.

The problem in 2D is defined on a rectangular fluid domain shown in Fig. 4 with an obstacle (a cylinder in 3D, or a circle in 2D) located 0.15 m away from the inlet., The cylinder is fixed and rigid. The no-slip boundary condition is imposed at the top and bottom container boundary, as well as on the surface of the obstacle (cylinder). The fluid enters the rectangular domain through the left side where the following Dirichlet boundary condition is imposed:

$$\boldsymbol{u} = \Big(\sin(\pi t/8)\big(6y(0.41-y)/(0.41)^2\big), 0\Big)^T, \quad 0 \le y \le 0.41, 0 \le t \le 8s. \tag{50}$$

The fluid outlet is the entire right side of the rectangular container, where the following outlet boundary conditions are prescribed for sub-problems (31) and (28):

$$\frac{\partial \boldsymbol{u}}{\partial \mathbf{n}} = 0 \text{ and } p = 0,$$

respectively.

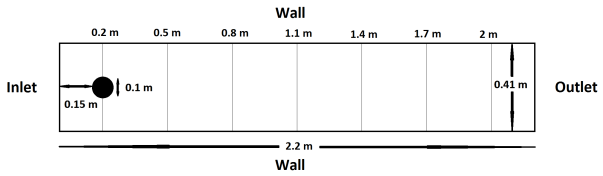

Figure 4: Schematic of $2D$ computational domain for flow past a cylinder. The vertical lines denote the locations in the domain where the horizontal component of flow rate was integrated to test mass conservation.

All the values in this benchmark problem are given in the SI units. The kinematic viscosity is $\nu = 10^{-3}$ m^2/s, and the fluid density is $\rho = 1.0$ kg/m^3. The maximum Reynolds number is around 100.

We used a triangular mesh with 1664 elements, shown Fig. 5 (top), with the basis functions of 4^{th} order, and time step $\Delta t = 10^{-4}$. Fig. 5 (bottom) illustrates the numerical results depicting the velocity vector field superimposed over the pressure contours at time $t = 8s$. A von Karman vortex sheet is captured in the channel.

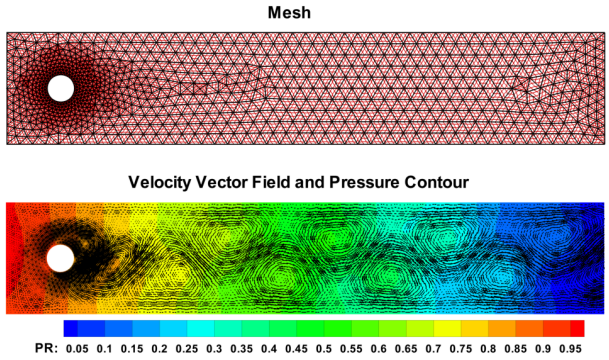

Figure 5: DG simulation of 2D flow past a cylinder: (top) 2D mesh consisting of 1664 elements and 4^{th} order polynomial bases, (bottom) Velocity vector field and pressure contours at time $t = 8s$.

Next, we carried out six simulations with different mesh and basis function settings, reported in Table 1. The maximum drag coefficient, lift coefficient and pressure difference between the front and back of the

Results	No. Dof	No. Elem.	Poly.	Max. Drag	Max. Lift	Δp at $t = 8$ s
h-refinement	9810	218	4	3.0278	0.4449	0.1021
	18360	408	4	3.0016	0.428	0.1075
	36360	808	4	2.96	0.3869	0.1072
	74880	1664	4	2.9444	0.3837	0.1075
p-refinement	35820	1194	3	2.9778	0.3890	0.1096
	53730	1194	4	2.9490	0.3872	0.107
	75222	1194	5	2.9446	0.3881	0.1073
	100296	1194	6	2.9446	0.3871	0.1074
Ref. [79]	(21508,667246)			(2.9220,3.8420)	(0.2649,1.1100)	(0.0200,0.1142)

Table 1: 2D simulation results compared to the values reported in Table 5 [79]. The interval values reported above correspond to the range of the values obtained in [79] with different solvers and finest meshes. We see that our results fall well within the values reported in [79].

cylinder were examined and compared with the values reported in Table 5 in [79]. The pressure difference

refers to the difference $\Delta p(t) = p(0.15, 0.2, t) - p(0.25, 0.2, t)$. Table 5 in [79] contains results obtained with 10 different approaches to numerically solving this problem. We report the intervals for the maximum drag coefficient, lift coefficient and pressure difference obtained with the finest meshes reported in Table 5 of [79], and compare those to our simulations. The results are show in Table 1. We see that our results fall well within the interval of values reported in [79]. Furtheromore, except for one simulation in [79], the number of degrees of freedom for our simulations were roughly one tenth of the degrees of freedom used with standard Finite Elements reported in [79].

Next, we considered a full $3D$ problem of flow past a cylinder with a circular cross-section. The fluid channel, shown in Fig. 6 (left), is defined by $0 \leq x \leq 1.5$ m, $-0.205 \leq y \leq 0.205$ m, $-0.205 \leq z \leq 0.205$ m, see [79, 11] . A cylinder of diameter 0.1 m is located at $x = 0.5$, $y = 0$, and $z = 0$. Similar to the 2D

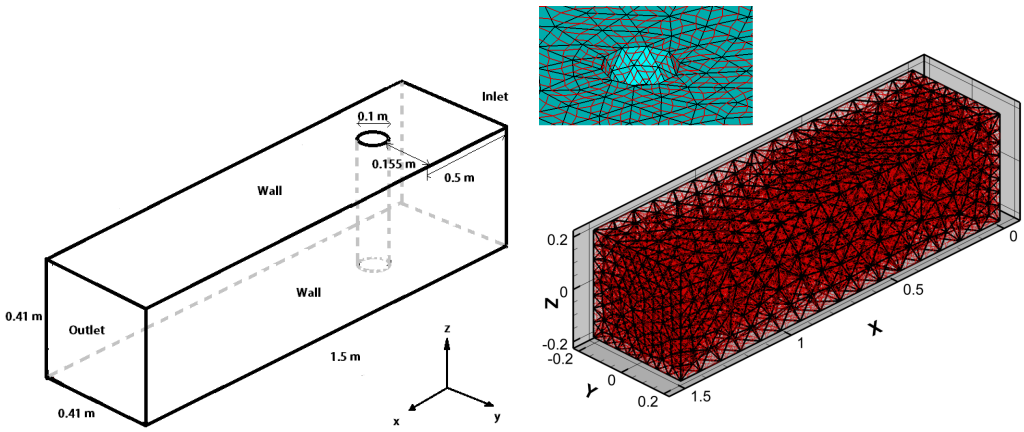

Figure 6: Left: Schematic of $3D$ computational domain for the flow past a cylinder. Right: a mesh of 5920 elements and 3^{rd} order of bases. The top panel on the right shows a size view of the mesh near the cylinder.

simulation, no-slip velocity boundary conditions are set at the channel walls and cylinder's surface. At the inflow side of the channel, see Fig. 6 (left), a Dirichlet boundary condition is prescribed with fluid velocity 0.45 m/s in the x direction. At the outflow, as in Sec. 5.1 $\frac{\partial u}{\partial \boldsymbol{n}} = 0$ and $p = 0$ are assumed. The kinematic viscosity is given by $\nu = 10^{-3}$ m^2/s, and the fluid density is $\rho = 1.0$ kg/m^3. The maximum Reynolds number is around 20.

Fig. 6 (right) shows a mesh of 5920 elements. Tetrahedral elements are depicted by black lines, while the interpolation points for 3^{rd} order bases are presented by the intersections of red lines. Our numerical results obtained with the mesh in Fig. 6 (right) are presented in Fig. 7, where contour plots of velocity in x direction are plotted, showing different slices of the velocity field.

Two simulations were performed with different levels of mesh refinement. The computed drag and lift coefficients, as well as the pressure difference $\Delta p = p(0.45, 0.20, 0.205, t) - p(0.55, 0.20, 0.205, t)$ between the front and back of the cylinder are compared to the results reported in [79, 11]. Table 2 lists the details of the simulations and compares them with the values reported in Table 7 of [79]. We report the intervals of the values for the drag, lift and pressure difference obtained in [79] with eight different numerical approaches and finest meshes. Again, very good match with the reference values can be observed, with a significantly smaller number of degrees of freedom.

Mass conservation. We use this example to test mass conservation of our DG solver. The cross-sectional average of the horizontal component of the velocity was calculated at 7 different cross-sections along the fluid domain, shown in Fig. 4, at 3 different times: $t = 2, 4, 6$ s. The times $t = 2, 6$ s were chosen symmetrically around the peak flow rate at $t = 4$ s associated with the sinusoidal inlet data given in (50). Since the fluid domain has rigid walls, we expect that the flow rate along the fluid domain remains constant if the mass is conserved, which is, indeed, the case in our simulations, as shown in Fig. 8(a). Notice how the graphs of the flow rates at $t = 2$ and $t = 6$ overlap in Fig. 8(a), as expected. A close inspection of

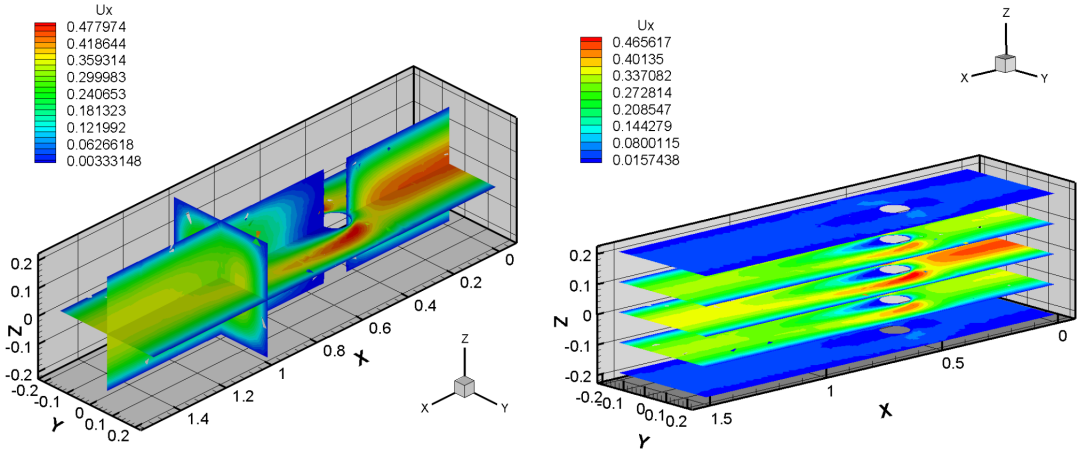

(a) $t = 4$ ms (b) $t = 6$ ms

Figure 7: 3D DG simulation of flow past a cylinder with the mesh in Fig. 6 (right): contour profile of velocity $\boldsymbol{u}$ in the x direction.

Results	Nodf	No. Elements	Poly.	Drag	Lift	Δp
	405720	2898	4	6.1059	0.0095	0.1611
	473600	5920	3	6.1105	0.0095	0.1613
Ref. [79]	2426292			(6.1043,6.1932)	(0.0010,0.010)	(0,1604,0.1709)

Table 2: 3D simulation results showing drag, lift and pressure difference compared to the values from Table 7 of [79]. The interval values quoted from Table 7 of [79] correspond to the results obtained with eight different numerical approaches, reported for finest meshes.

the relative error in mass conservation is shown in Fig. 8(b), where the numerically calculated flow rate is compared with the exact flow rate, obtained from the prescribed inlet data. We see that the relative error in absolute value is less than 0.4%, which shows excellent mass conservation properties of this scheme.

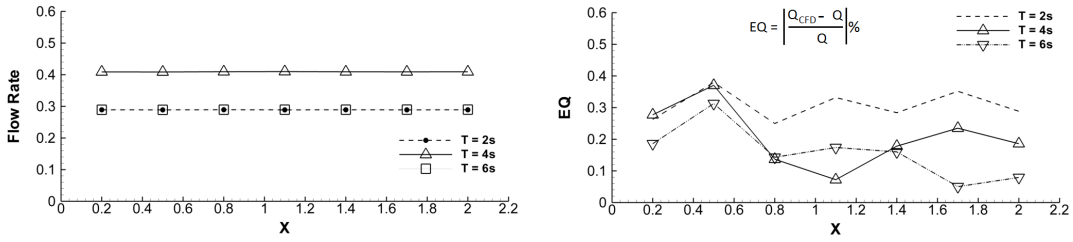

(a) Flow rate (b) Percentage error in mass conservation

Figure 8: Benchmark test 1: (a) flow rate and (b) percentage error in mass conservation reported at 7 different locations along the fluid domain, and three different times $t = 2, 4, 6$ s. We see that mass conservation error is below 0.4%.

5.2. Benchmark test 2: Compliant vessel

We consider the classical FSI test problem proposed in [43]. This benchmark has been used for testing the results of fluid structure interaction algorithms by several authors [5, 16, 48, 73]. The structure model for this benchmark problem is given by eq. (13) with absorbing boundary conditions (15),(16).

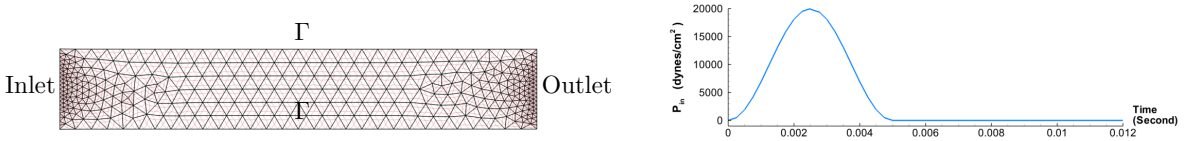

(a) Computational domain showing computational mesh

(b) Inlet data.

Figure 9: Benchmark test 2: (a) computational domain at the initial time with an unstructured triangle mesh (fine mesh) and (b) inlet pressure pulse as a function of time.

The reference computational domain is a 6 cm $\times$ 1 cm rectangle shown in Fig. 9(a). The top and bottom walls are deformable. Neumann boundary conditions are imposed at the inlet and the outlet:

$$\boldsymbol{\sigma n}|_{\Gamma_{in}} = -p_N \boldsymbol{n} = -\frac{P_{max}}{2}\left[1 - \cos\left(\frac{\pi t}{2.5}\right)\right]\boldsymbol{n}, \tag{51}$$

$$\boldsymbol{\sigma n}|_{\Gamma_{out}} = -p_N \boldsymbol{n} = \boldsymbol{0}, \tag{52}$$

where

$$P_{max} = \begin{cases} 2 \cdot 10^4 \text{ dynes/cm}^2, & t \leq 5 \text{ ms}, \\ 0, & t > 5 \text{ ms}. \end{cases}$$

See Fig. 9(b). The values of all the parameters in the structure model are given in Tables 3.

Table 3: Structural parameters for benchmark test 2.

Structure density	$\rho_s = 1.1$ g/cm^3	Wall thickness	$h_s = 0.1$ cm
Timoshenko shear factor	$k = 1$	Young modulus	$E = 0.75 \times 10^6$ dynes/cm^2
Shear modulus	$G = \frac{E}{2(1+\nu)} = 0.25 \times 10^6$ dynes/cm^2	Viscoelastic parameter	$\gamma = 0.01$
Poisson ratio	$\nu_s = 0.5$	Reference radius	$R_0 = 0.5$ cm

Two unstructured triangular meshes are used: a coarse mesh with 282 triangles and a fine mesh with 684 triangles. The fine mesh is shown in Fig. 9(a). The time interval under consideration is $[0, 12]$ ms. The time step is set to $2.5 \cdot 10^{-4}$ s for the coarse mesh and to 10^{-4} s for the fine mesh. For this test, we use the Dirichlet-Neumann algorithm and the nodal DG method discussed in Sec. 3 with third order Lagrangian basis functions. The numerical results given by our DG solver with IP fluxes were compared with the numerical results obtained using the monolithic scheme presented in [72, 6]. The results in [72, 6] were obtained using a mesh comparable to the fine mesh used here and time step 10^{-4} s.

Fig. 10 shows the propagation of the pressure wave in the 2D tube, obtained using our solver. A detailed comparison between the pressure evaluated along the center line at six different times between our simulations and the results of [72, 6] is shown in Fig. 11. This figure also shows our results obtained at the coarse and fine mesh, which are almost indistinguishable. We see excellent agreement with the results reported in [72, 6].

5.3. Benchmark test 3: Stationary linearly elastic 1D membrane bubble

In this section we consider a benchmark test with a pressure discontinuity. The goal is to validate the implementation of the Robin-Neumann algorithm and to show that our DG method is able to correctly capture the pressure discontinuity.

The test, inspired by an example in [10], consists of trying to recover a steady-state solution that develops after a circular membrane of radius 1, immersed in a fluid at rest, is exposed to a pressure jump that causes

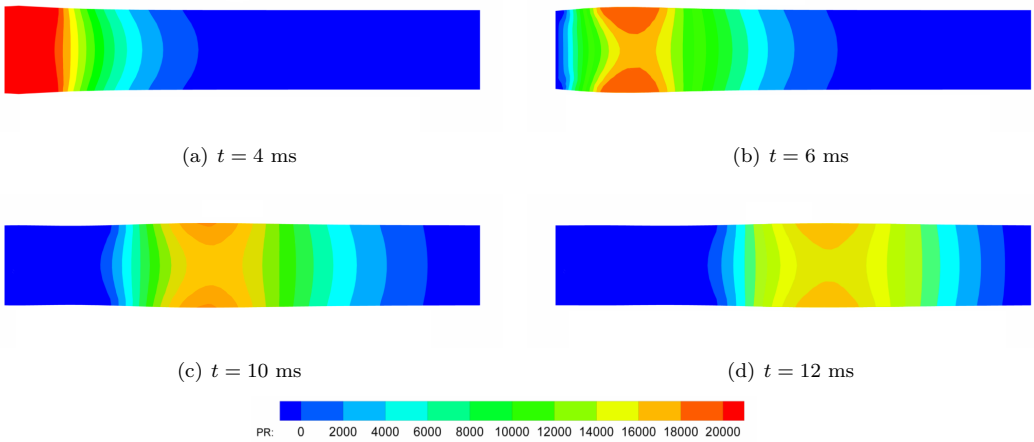

(a) $t = 4$ ms (b) $t = 6$ ms

(c) $t = 10$ ms (d) $t = 12$ ms

Figure 10: Benchmark test 2: Pressure wave at four times: (a) $t = 4$ ms, (b) $t = 6$ ms, (c) $t = 10$ ms, and (d) $t = 12$ ms.

the membrane to stretch and approach a steady state which is a circle of radius R, where R is determined from the pressure jump and the elastic properties of the membrane.

More precisely, we consider the fluid domain to be a rectangle $\Omega = (-2, 2) \times (-2, 2)$ cm, and we consider a fluid with density $\rho = 1$ g/cm^3, and viscosity $\mu = 1$ g/(cm s). The structure, i.e., the closed elastic membrane immersed in the fluid, is set initially to be a circle of radius 1 centered at the origin, parameterized by $s \in [0, 2\pi)$:

$$\boldsymbol{x}_0(s) = (\cos(s), \sin(s))^T, \qquad s \in [0, 2\pi). \tag{53}$$

The circular membrane is exposed to a pressure jump $[\![p]\!] = 1$ dyne/cm^2, and the membrane stretches from its reference configuration $\boldsymbol{x}_0$ to a new position $\boldsymbol{x}$, which is obtained by solving the structure model (12), (17) with $C_x = C_y =: C = 10$ dynes/cm^3, and $\rho_s h_s = 1$ g/cm^2. The displacement is given $\boldsymbol{\eta} = \boldsymbol{x} - \boldsymbol{x}_0$.

To get to the steady state, we are numerically solving the following a FSI problem where the structure is modeled by:

$$\rho_s h_s \frac{\partial^2 \boldsymbol{x}(s,t)}{\partial t^2} + C\boldsymbol{x}(s,t) = [\![p]\!]\boldsymbol{n} + C\boldsymbol{x}_0,$$

with $\boldsymbol{x}(2\pi) = \boldsymbol{x}(0)$. The steady-state solution of the FSI problem is given by:

$$\boldsymbol{x} = \Big(1 + \frac{[\![p]\!]}{C}\Big)\boldsymbol{x}_0, \text{ or } \boldsymbol{\eta} = \frac{[\![p]\!]}{C}\boldsymbol{x}_0, \ \boldsymbol{u} = \boldsymbol{0}, \ p(\boldsymbol{x}) = \begin{cases} 1 \text{ dynes/cm}^2 & \text{inside the membrane,} \\ 0 \text{ dynes/cm}^2 & \text{outside the membrane.} \end{cases} \tag{54}$$

Thus, the steady-state solution consists of a circular membrane of radius $1 + \frac{[\![p]\!]}{C} = 1.1$ cm, immersed in the fluid at rest, with the fluid pressure inside the membrane equal to 1 dyne/cm^2, and outside 0 dyne/cm^2.

To solve this problem numerically, we consider the unstructured mesh shown in Fig. 12(a), which has 180 triangles and is aligned with the membrane. A seventh order Lagrangian basis is used for the fluid, structure, and ALE problem. The time step is set to $\Delta t = 0.002$ s, initial velocity to $\boldsymbol{u} = \boldsymbol{0}$ cm/s, and initial structure position given by (53). Fig. 12(b) and (c) shows the velocity magnitude and pressure at $t = 0.1$ s, i.e. after 50 steps, calculated using the Robin-Neumann algorithm. We see in Fig. 12(c) that the pressure jump is perfectly resolved. The velocity magnitude displayed in Fig. 12(b) is around 10^{-5} cm/s in most of the domain. Slightly larger values of the velocity magnitude (around 10^{-4} cm/s) can be observed close to the 1D membrane. This is due to the fact that the exact solution for the membrane position, i.e. a circle, is approximated with a piecewise polynomial of degree seven. Thus, the exact velocity is approximated up to a discretization error.

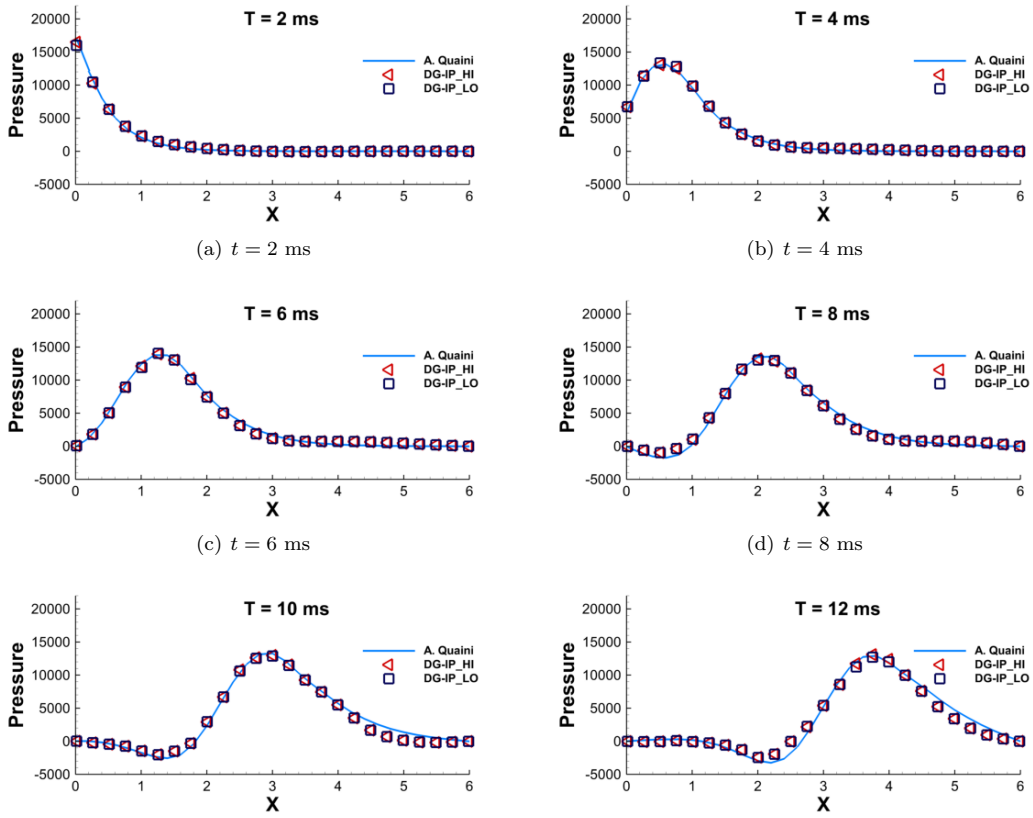

(a) $t = 2$ ms (b) $t = 4$ ms

(c) $t = 6$ ms (d) $t = 8$ ms

(e) $t = 10$ ms (f) $t = 12$ ms

Figure 11: Benchmark test 2: Pressure (dynes/cm^2) along the centerline at times: (a) $t = 2$ ms, (b) $t = 4$ ms, (c) $t = 6$ ms, (d) $t = 8$ ms, (e) $t = 10$ ms, (f) $t = 12$ ms. As shown in the legend, the blue line denotes the results obtained in [72, 6], while the red triangles and blue squares denote the results obtained with our DG solver with IP fluxes, using the fine and coarse mesh, respectively.

This example shows that our methodology captures the correct steady-state solution, and that the jump in the pressure is well resolved.

5.4. Benchmark test 4: Oscillating immersed linearly elastic 1D membrane bubble

The goal of this test, also inspired by the work in [10], is to verify convergence of the algorithm and the mass conservation with respect to mesh refinement.

For this purpose we consider the same linearly elastic circular membrane, as in the benchmark test 3, discussed in Sec. 5.3, where the membrane is immersed in an incompressible, viscous fluid with viscosity $\mu = 0.2$ g/cm s, occupying the rectangle $\Omega = (-2.5, 2.5) \times (-2.5, 2.5)$ cm. However, we are interested in studying the membrane oscillations that are induced by its initial shape, which is an ellipse, given by:

$$\boldsymbol{\eta}(s) = \Big((a-1)\cos(s), (1.21/a - 1)\sin(s)\Big)^T, \qquad s \in [0, 2\pi], \tag{55}$$

where $a = 1.5$. Here the displacement is again measured from the reference configuration, which is a circle of radius 1. We impose the same periodic boundary condition as in Sec. 5.3. Due to the elastic forces, the membrane will oscillate and eventually converge to its equilibrium configuration, which is determined by the

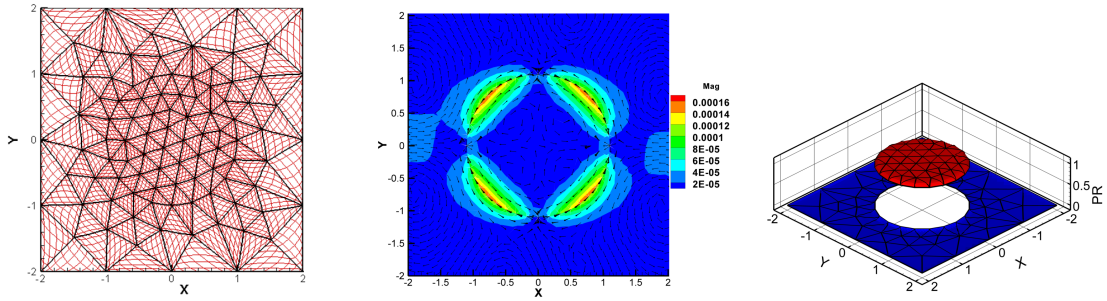

(a) Mesh (b) Velocity magnitude and vector field (c) Pressure discontinuity

Figure 12: Benchmark test 3: (a) Unstructured triangular mesh used for the computations; (b) Velocity magnitude and vector field at $t = 0.1$ s; (c) Pressure jump at $t = 0.1$ s.

jump between the interior and exterior pressure, equal to 1 dyne/cm^2, and by the spring constant $C = 10$ dyne/cm^3. Thus, again, the equilibrium state is given by the membrane assuming a circular shape of radius 1.1 cm. However, due to the elliptical initial state, the membrane will oscillate, as shown in Fig. 13, until it reaches the equilibrium state. We will track the maximum x coordinate of the membrane, and compare the behavior of the oscillations of the x coordinate for different mesh refinements.

We solve the coupled FSI problem with the Robin-Neumann algorithm. The whole computational domain consists of the sub-domains: Ω_1, and Ω_2, and the boundary Γ_t separating the two fluid domains. Domain Ω_1 represents the exterior fluid domain, Ω_2 the interior fluid domain (the bubble), and Γ_t the elastic membrane. The following boundary conditions for velocity and pressure are assigned on each boundary:

- on the outer boundary of Ω_1 (the square boundary), boundary conditions (30) with $p_N = 0$ and (33) are prescribed;
- on Γ_t, considered as the remaining part of the boundary of Ω_1, equations (29) and (49) are prescribed;
- on Γ_t considered as the boundary of Ω_2, equations (48) and (49) are prescribed.

Two meshes are considered: a coarse mesh with 6416 triangles and a fine mesh with 8980 triangles. The latter mesh is shown in Fig. 13(a). In both cases we use quadratic polynomial bases and time step $\Delta t = 0.01$ s.

Fig. 13(b)-(f) shows pressure contour computed with the fine mesh at six different times. We see that the membrane, initially elliptic, oscillates until it reaches a circular shape around time $t = 8$ s. Fig. 14(a) reports the maximum x-coordinate of the structure position over time. We see that the maximum x-coordinate evolves towards 1.1 cm through damped oscillations, as expected since the stationary solution for the membrane is the circle of radius 1.1 cm centered at the origin. Fig. 14(a) also shows that the two simulations, performed for two different meshes, are almost identical. A magnified view of the absolute value of the difference between the two simulations is shown in Fig. 14(b), indicating the maximum difference between the two simulations of 0.6%.

Mass conservation. We shown in this example that our method approximates well the mass conservation property. We tested the change in area inside the membrane over time. Since the fluid is incompressible, and there are no sources or sinks of fluid inside the membrane, the volume (area) of the "bubble" must be conserved. Indeed, in Fig. 15 we show the relative difference in the "bubble" area in absolute value over time for two different meshes. We first observe that as the mesh gets refined, the mass conservation property is better approximated. Secondly, we observe that the mass conservation error is less than 0.7% for the fine mesh, indicating that our FSI solver satisfies well the mass conservation property.

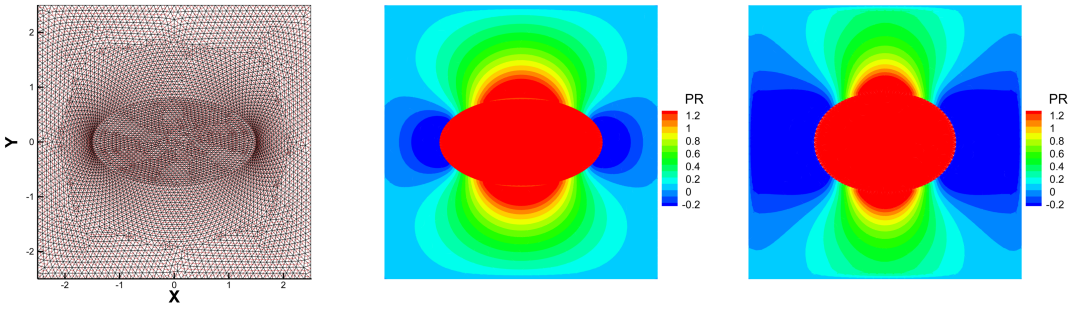

(a) fine mesh (b) $t = 0.1$ s (c) $t = 0.5$ s

(d) $t = 1$ s (e) $t = 2$ s (f) $t = 8$ s

Figure 13: Benchmark test 4: (a) fine mesh (6416 elements) at time $t = 0.1$ s and the pressure contour at times: (b) $t = 0.1$ s, (c) $t = 0.5$ s, (d) $t = 1$ s, (e) $t = 2$ s, and (f) $t = 8$ s.

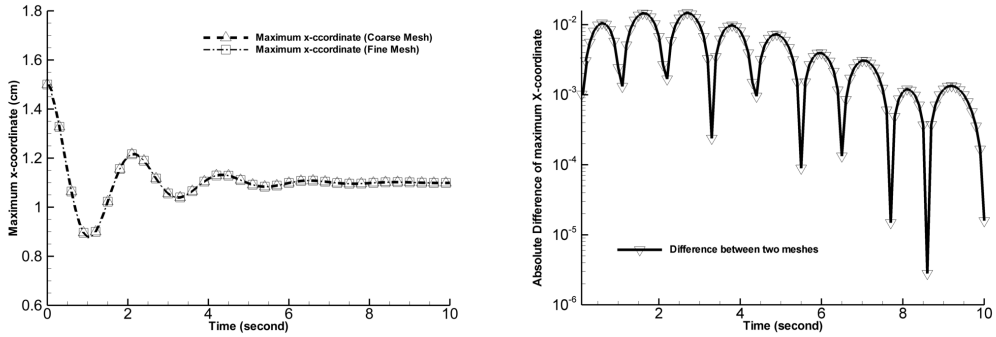

(a) Maximum x-coordinate over time. (b) Difference.

Figure 14: Benchmark test 4: Comparison between solutions at two different meshes (coarse (6416 elements) and fine (8980 elements)). (a) Oscillations of the maximum x-coordinate over time plotted for two different meshes. The results are almost identical. (b) Difference in absolute value between the two curves plotted in (a). The maximum difference for the two different meshes is 0.6%.

5.5. Abdominal Aortic Aneurysm

We conclude this manuscript by applying the methodology presented above on the simulation of blood flow through a patient-specific aortic abdominal aneurysm (AAA) before and after treatment with a vascular prosthesis called stent-graft.

As mentioned in Sec. 1, aortic abdominal aneurysm, shown in Fig. 1, is an enlargement of the abdominal

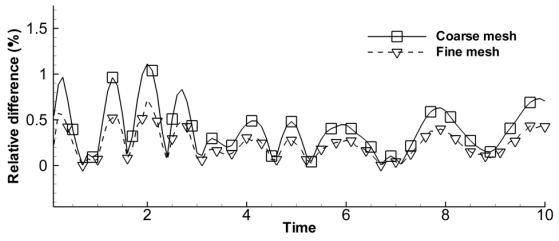

Figure 15: Benchmark test 4. Mass conservation test: relative difference in the "bubble" area in absolute value for two different meshes.

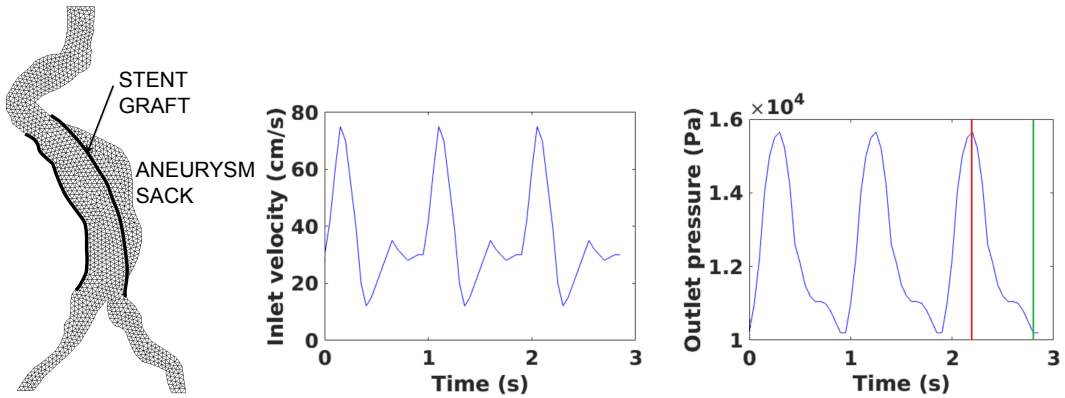

Figure 16: Left: Patient-specific AAA computational mesh with a delineated stent-graft location used in our simulations. Middle and right: Inlet data (velocity) and outlet data (pressure). The red and green lines in the pressure data correspond to the times when the pressure, velocity, and displacement are reported in Figs. 17 and 18 below (systole and diastole, respectively).

aorta, which may rupture and be fatal. Treatment entails excluding the aneurysm from circulation by implanting a device called stent-graft, pictured in Fig. 1. One of the goals of the treatment is to lower the pressure on the aneurysm walls and thereby minimize the probability of AAA rupture. The goal of this section is to simulate the flow and the pressure wave exerted by the time-dependent blood flow on the aneurysm walls before and after the implantation of stent-graft in order to understand the benefits of the stent-graft implantation. For this purpose we consider a section of a patient-specific AAA geometry, with the corresponding computational domain shown in Fig. 16 (left), obtained from a 3D reconstruction of the in-vivo acquired CT scans, presented in [82]. The inlet is at the top of the domain, corresponding to the proximal section of the patient's abdominal aorta, and exits from the two outlet sections at the bottom of the computational geometry, corresponding to the iliac arteries. We consider this geometry without and with an implanted stent-graft. The location of the stent-graft is sketched in Fig. 16 (left). The lateral walls of the entire computational domain are considered elastic, as well as the walls of the stent-graft. The elastic membrane model in (12) and (17) is used to model both elastic structures. The flow inlet is aligned with the y-axis, and the elastic walls are assumed to displace in both x and y direction. The density and spring constants of the AAA walls and of the stent-graft are assumed to be the same: $\rho_s = 1$ g/cm^3 and $C_x = C_y = 1.0 \times 10^5$ dynes/cm^3. The fluid has the same density and viscosity as in the Sec. 5.2. In the region where the stent-graft overlaps the aortic wall, the spring constant's value are given by the sum of the spring constants of the two elastic materials. At the inlet section, we specify a parabolic velocity profile with the average velocity reported in Fig. 16(a). At the outlet sections, we impose a non-homogeneous Neumann condition with the given data as shown in Fig. 16(b). The data in Fig. 16, which spans three cardiac cycles, is taken from [66] and rescaled in order to have a peak Reynolds number of roughly 1800. In

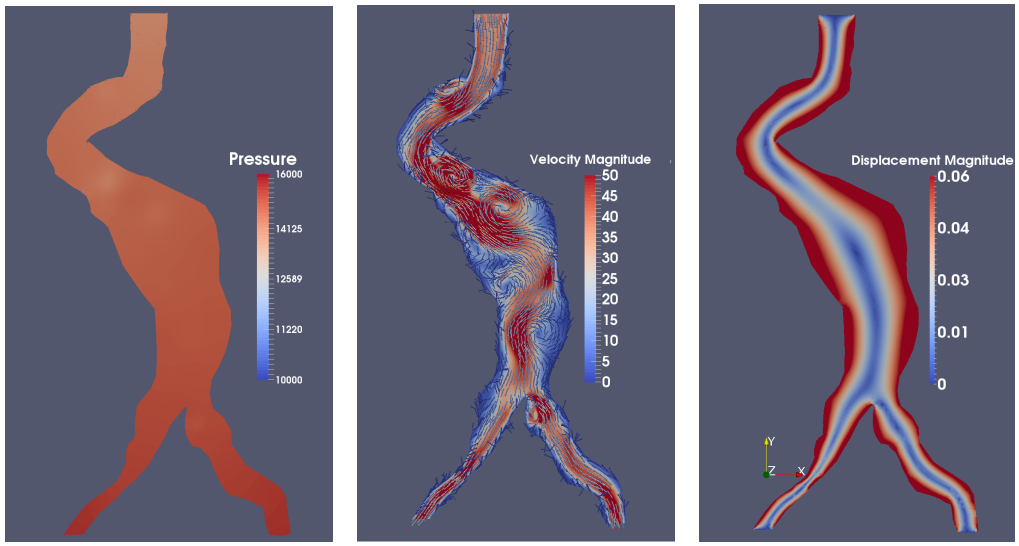

(a) p without stent graft (b) $||\boldsymbol{u}||$ without stent graft (c) $||\boldsymbol{d}||$ without stent graft

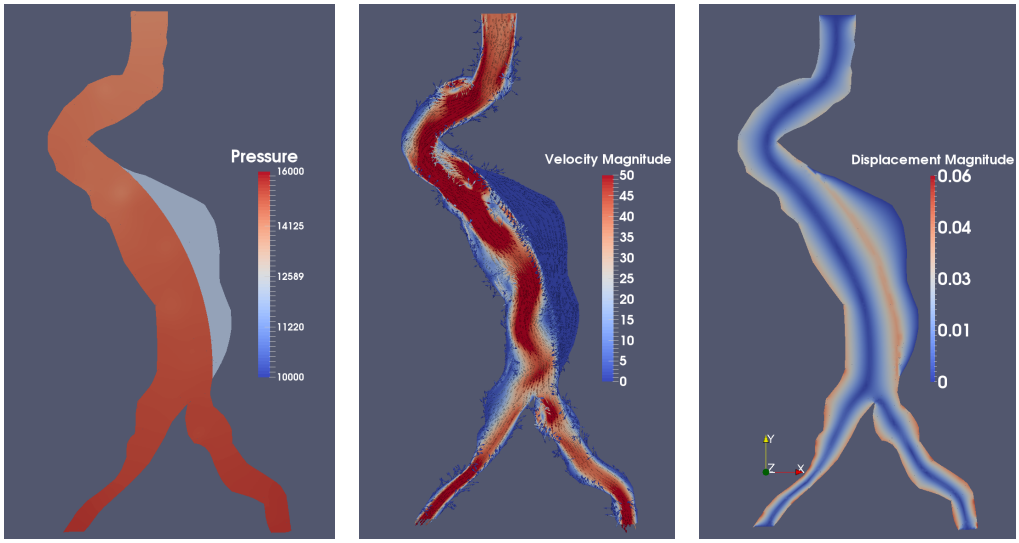

(d) p with stent graft (e) $||\boldsymbol{u}||$ with stent graft (f) $||\boldsymbol{d}||$ with stent graft

Figure 17: Numerical simulation of flow in Aortic Abdominal Aneurysm before and after the implantation of a sent-graft. The top and bottom rows correspond to AAA before and after the placement of the stent-graft, respectively. Panels (a) and (d) show the pressure, (b) and (e) velocity magnitude and vector field, and (c) and (f) displacement magnitude at time $t = 2.3$ s.

fact, the maximum Reynolds number inside AAA is normally between 1500 and 2000 [41, 68, 67, 26]. The external pressure of $p_{ext} = 12000$ Pa is used to model the surrounding pressure. This value corresponds to the average pressure, i.e., the minimum outlet pressure plus one third of the pressure difference between the maximum and minimum outlet pressure in one cardiac cycle.

For the case without a stent graft we used the Dirichlet-Neumman method to solve the FSI problem, while for the case with a stent graft we had to use the Robin-Neumann scheme since the problem contains a fluid region that is entirely surrounded by an elastic structure. This is because the stent graft divides the

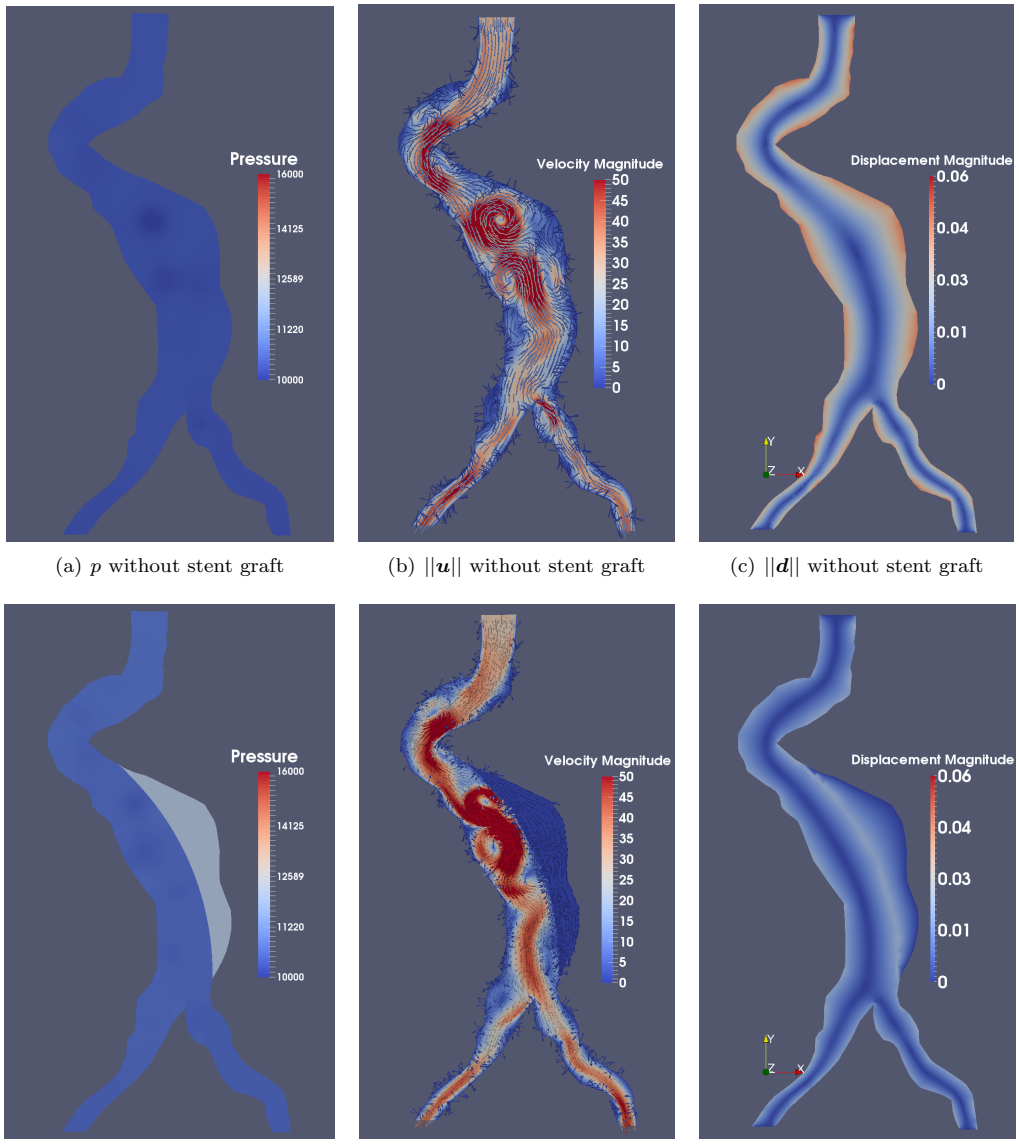

(a) p without stent graft (b) $||\boldsymbol{u}||$ without stent graft (c) $||\boldsymbol{d}||$ without stent graft

(d) p with stent graft (e) $||\boldsymbol{u}||$ with stent graft (f) $||\boldsymbol{d}||$ with stent graft

Figure 18: Numerical simulation of flow in Aortic Abdominal Aneurysm before and after the implantation of a sent-graft. The top and bottom rows correspond to AAA before and after the placement of the stent-graft, respectively. Panels (a) and (d) show the pressure, (b) and (e) velocity magnitude and vector field, and (c) and (f) displacement magnitude at time $t = 2.85$ s.

fluid domain into two subdomains: the lumen and the aneurism sack, the latter being a closed domain.

The following boundary conditions for the pressure and velocity are assigned for this problem:

- On the AAA walls, conditions (48) and (49) are prescribed with $p_k^+ = p_{ext}$.
- On the exterior boundary of the aneurism sack, conditions (29) and (49) are prescribed.
- On the interior boundary of the aneurism sack, conditions (48) and (49) are prescribed.

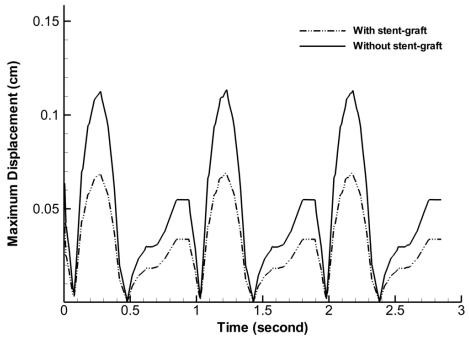

Figure 19: Maximum displacement magnitude of the aneurysm wall over time (3 cycles) without and with stent graft.

Using the proposed DG method for this problem provides a sharp resolution of the pressure jump that occurs across the stent graft, between the fluid occupying the lumen and the fluid in the aneurysm sack. An unstructured mesh with 2297 triangles, reported in Fig. 16 (left), was used in the simulations, with a third order Lagrangian basis for the fluid, structure, and ALE problem. The number of degrees of freedom for the fluid problem is only 62×10^3. Three cardiac cycles where simulated, corresponding to 2.85 s of physical time, with $\Delta t = 0.00025$ s. This took around 12 hours on a i5 CPU and 16GB memory desktop.

Fig. 17 shows the pressure, velocity magnitude, velocity vector field, and displacement magnitude without and with the stent graft inserted into AAA, at time $t = 2.3$ s, which is the time in systole when the pressure at the iliac arteries reaches its maximum. Fig. 18 shows the same plots except at time $t = 2.85$ s, which is the time in diastole when the pressure at the iliac arteries reaches the minimum. Comparing the velocity magnitude sub-plots (b) and (e) in both Figs. 17 and Fig. 18, we see that after the stent graft implantation the vortices are inhibited and confined. In particular, during systole, shown in Fig. 17, we see almost laminar flow through the stented AAA, with significant reduction in vortex formation. Even more importantly, panels (a) and (d) in Figs. 17 and 18 show significant reduction in the pressure exerted onto the aneurysm sack walls, which results in reduction of AAA pulsation (periodic displacement/deformation of AAA walls), as shown in panels (c) and (f), after the insertion of the stent-graft.

The maximum displacement magnitude over time with and without the stent-graft is reported in Fig. 19, which reveals that the presence of the stent-graft makes the displacement magnitude of the AAA sack roughly 50% smaller.

This example shows that the proposed computational method can be successfully used to investigate which stent graft is better for a given patient-specific geometry. The geometry of AAA, the material properties and geometry of the stent-graft will all influence the pressure reduction of a given patient-specific AAA.

5.6. Preliminary FSI results in 3D

We conclude this paper by presenting numerical results showing blood flow in a 3D patient-specific AAA, shown in Fig. 20. With this example we show that the method considered in this manuscript can be successfully extended to 3D. Furthermore, to emphasize the importance of assuming compliant AAA walls in correctly capturing the pressure wave propagation, we also include the simulation with rigid walls, which shows a significantly different pressure distribution in AAA walls, as expected.

We set the blood density and viscosity to $\rho = 1$ g/cm^3 and $\mu = 0.035$ cm^2/s, respectively. At the fluid inlet and outlet sections (see Fig. 20(a)) we impose the boundary conditions in (51),(52) with

$$P_{max} = \begin{cases} 1.5 \cdot 10^4 \text{ dynes/cm}^2, & t \leq 5 \text{ ms}, \\ 0, & t > 5 \text{ ms}. \end{cases}$$

The inlet pressure pulse is shown in Fig. 21, where the red dots indicate the times at which the snap-shots

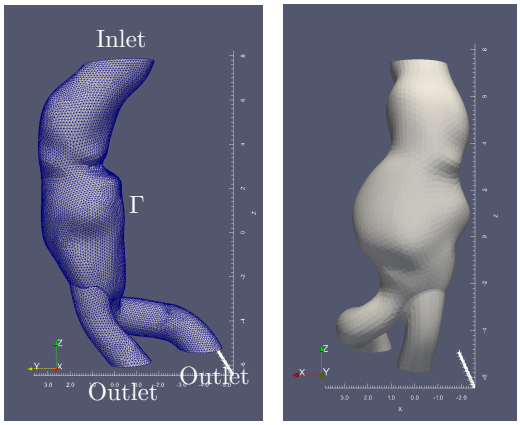

Figure 20: Two views of the reference AAA domain, with computational mesh shown in the figure on the left.

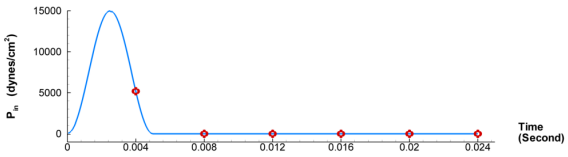

Figure 21: Inlet pressure pulse. The red dots indicate the times at which the pressure is plotted in Fig. 22.

showing pressure wave propagation are taken in Fig. 22.

The aneurysm wall is modeled by (12),(17). We enforce zero displacements at both the proximal and distal region (descending aorta and iliac arteries respectively, see Fig. 20(a)). The density, thickness and Young's modulus of the aneurysm are set to $\rho_s = 1$ g/cm^3, $h_s = 0.1$ cm and $E = 1 \times 10^5$ dynes/cm^2, respectively.

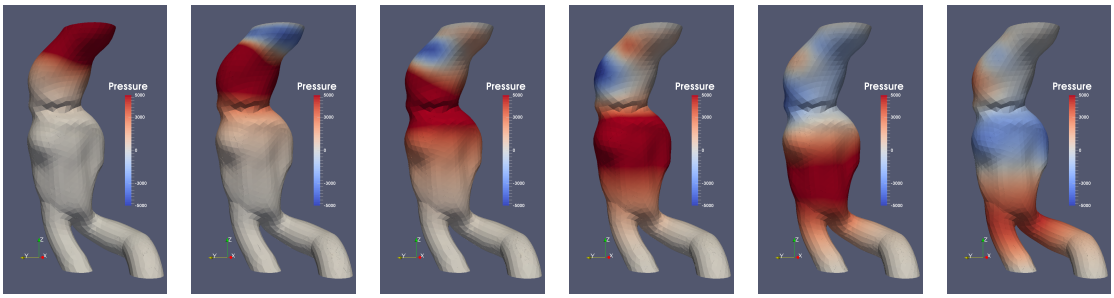

(a) $t = 4$ ms (b) $t = 8$ ms (c) $t = 12$ ms (d) $t = 16$ ms (e) $t = 20$ ms (f) $t = 24$ ms

Figure 22: Snapshots of the pressure ($dynes/cm^2$) propagation inside the AAA at six different times: (a) $t = 4$ ms, (b) $t = 8$ ms, (c) $t = 12$ ms, (d) $t = 16$ ms, (e) $t = 20$ ms, (f) $t = 24$ ms. The times correspond to the red dots in Fig. 21.

We considered the unstructured mesh shown in Fig. 20(a), which consist of 47192 tetrahedra, and second order Lagrange bases for the fluid, structure, and ALE problem. The total number of degrees of freedom for the fluid problem is 1,887,680. We let the simulation run from 0 to 24 ms with time step $\Delta t = 0.0001$ s. The simulation takes 2 hours 45 minutes on a i5 and 64GB memory desktop. Fig. 22 shows the pressure computed by the Dirichlet-Neumann scheme at six different times corresponding to the red dots in Fig. 21.

We clearly see the propagation of the pressure pulse in the fluid domain.

Finally, we compare these simulations with the case when the AAA walls are rigid. We expect in this case to see close to linear pressure distribution between the inlet and outlet data, with zero pressure in the entire domain occurring when the inlet and outlet data both assume zero values, which is immediately after 4 ms. Indeed, in Fig. 23(a) we see an almost linear pressure distribution between the inlet and outlet for $t = 4$ ms, and zero pressure everywhere in the fluid domain at time $t = 8$ ms shown in panel (b). A direct comparison with the case of compliant walls, shown in Fig. 23, shows very different solutions. Compliant walls support pressure wave propagation, whose speed depends on the elastic properties of the AAA walls.

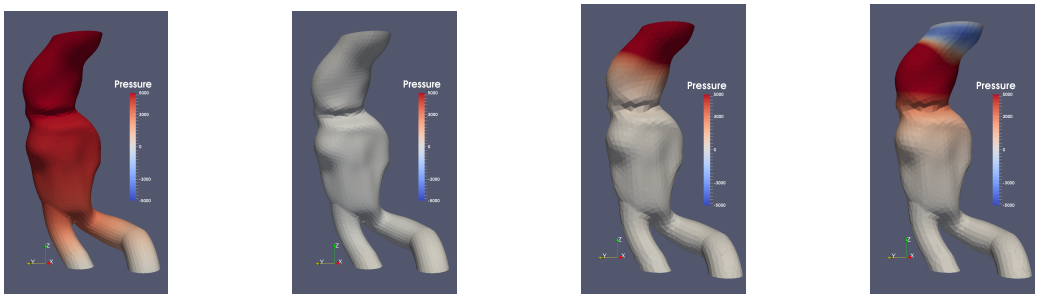

(a) t=4ms (RIGID) (b) t=8ms (RIGID) (c) $t = 4$ ms (COMPLIANT) (d) $t = 8$ ms (COMPLIANT)

Figure 23: Comparison in pressure wave propagation between rigid (panels (a) and (b)) and compliant walls (panels (c) and (d)). The prescribed inlet normal stress is depicted in Fig. 21, and the outlet normal stress is zero. Pressure exerted to the aneurysm walls at times $t = 4$ ms and $t = 8$ ms is shown. For $t \geq 8$ ms the pressure in the rigid case is equal to zero.

6. Conclusion and Outlook

In this work we presented a higher-order DG method with interior penalty, combined with an ALE approach and two strongly-coupled partitioned schemes (the Dirichlet-Neumann and Robin-Neumann schemes) to study fluid-structure interaction problems between incompressible, viscous fluids and elastic structures. The main reasoning behind considering a DG framework in the context of incompressible fluids is the need for a sharp resolution of the jump in the normal stress across fluid-structure and structure-structure interfaces that normally arises in this class of problems. More generally, when thick structures are considered (finite elasticity) in the context of nonlinear elasticity, shock wave solutions might occur within structures themselves. In this case the proposed framework would naturally extend to simulating the elastodynamics of nonlinearly elastic structures, and would present a unified approach to solving the entire FSI problem in a way that would resolve jump discontinuities naturally arising at the interfaces and within structures themselves.

Acknowledgments

This research has been supported in part by the National Science Foundation under grants DMS-1613757 (Canic), DMS-1318763 (Canic and Wang), DMS-1311709 (Canic), DMS-1263572 (Canic, Quaini and Wang), DMS-1109189 (Canic and Quaini), DMS-1620384 (Quaini).

References

[1] D. Arnold. An interior penalty finite element method with discontinuous elements. *SIAM J. Numer. Anal.*, 19:742–760, 1982.

[2] D.N. Arnold, F. Brezzi, B. Cockburn, and L.D. Marini. Unified analysis of discontinuous galerkin methods for elliptic problems. *SIAM J Numer. Analys.*, 39:1749–1779, 2002.

[3] M. Astorino, F. Chouly, and M.A. Fernández Varela. Robin based semi-implicit coupling in fluid-structure interaction: Stability analysis and numerics. *SIAM J. Sci. Comput.*, 31:4041–4065, 2009.

[4] F.P.T. Baaijens. A fictitious domain/mortar element method for fluid-structure interaction. *Int. J. Numer. Meth. Fluids*, 35:743–761, 2001.

[5] S. Badia, F. Nobile, and C. Vergara. Fluid-structure partitioned procedures based on Robin transmission conditions. *J. Comput. Phys.*, 227:7027–7051, 2008.

[6] S. Badia, A. Quaini, and A. Quarteroni. Modular vs. non-modular preconditioners for fluid-structure systems with large added-mass effect. *Computer Methods in Applied Mechanics and Engineering*, 197(49-50):4216–4232, 2008.

[7] S. Badia, A. Quaini, and A. Quarteroni. Splitting methods based on algebraic factorization for fluid-structure interaction. *SIAM J. Sci. Comput.*, 30(4):1778–1805, 2008.

[8] J. Banks, W. Henshaw, and D. Schwendeman. An analysis of a new stable partitioned algorithm for FSI problems. Part I: Incompressible flow and elastic solids. *Journal of Computational Physics*, 269:108–137, 2014.

[9] J. Banks, W. Henshaw, and D. Schwendeman. An analysis of a new stable partitioned algorithm for FSI problems. Part II: Incompressible flow and structural shells. *Journal of Computational Physics*, 268:399–416, 2014.

[10] S. Basting, A. Quaini, R. Glowinski, and S. Canic. An extended ale method for fluid-structure interaction problems with large structural displacements. *Journal of Computational Physics*, (331):312–336, 2017.

[11] E. Bayraktar, O. Mierka, and S. Turek. Benchmark computations of 3d laminar flow around a cylinder with cfx, openfoam and featflow. *Int. J. of Computational Science and Engineering*, 7:253–266, 2012.

[12] Y. Bazilevs, V.M. Calo, Y. Zhang, and T.J.R. Hughes. Isogeometric fluidstructure interaction analysis with applications to arterial blood flow. *Comput. Mech.*, 38:310–322, 2006.

[13] Y. Bazilevs, M.C. Hsu, Y. Zhang, W. Wang, X. Liang, T. Kvamsdal, R. Brekken, and J.G. Isaksen. A fully-coupled fluid-structure interaction simulation of cerebral aneurysms. *Comput. Mech.*, 46:3–16, 2010.

[14] M. Bukac and S. Canic. Longitudinal displacement in viscoelastic arteries: a novel fluid-structure interaction computational model, and experimental validation. *Journal of Mathematical Biosciences and Engineering*, 10(2):258–388, 2013.

[15] M. Bukac, S. Canic, R. Glowinski, B. Muha, and A. Quaini. A modular, operator-splitting scheme for fluid-structure interaction problems with thick structures. *International Journal for Numerical Methods in Fluids*, 74(8):577–604, 2014.

[16] M. Bukac, S. Canic, R. Glowinski, J. Tambaca, and A. Quaini. Fluid-structure interaction in blood flow capturing non-zero longitudinal structure displacement. *Journal of Computational Physics*, 235:515–541, 2013.

[17] M. Bukac, S. Canic, and B. Muha. A partitioned scheme for fluid-composite structure interaction problems. *Journal of Computational Physics*, 281(0):493 – 517, 2015.

[18] M. Bukac and B. Muha. Stability and convergence analysis of the kinematically coupled scheme for fluid-structure interaction. *SIAM Journal on Numerical Analysis*, 54(5):3032–3061, 2016.

[19] C. Grandmont C. Farhat, P. Geuzaine. The discrete geometric conservation law and the nonlinear stability of ALE schemes for the solution of flow problems on moving grids. *Journal of Computational Physics*, 174:669–694, 2001.

[20] S. Canic, B. Muha, and M. Bukac. Fluid-structure interaction in hemodynamics: Modeling, analysis, and numerical simulation. In *Fluid-Structure Interaction and Biomedical Applications (Bodnar, Galdi, Necasova eds.)*, Advances in Mathematical Fluid Mechanics. Birkhauser Basel, 2014.

[21] S. Canić, B. Muha, and M. Bukač. Stability of the kinematically coupled β-scheme for fluid-structure interaction problems in hemodynamics. *Journal for Numerical Analysis and Modeling*, 12(1):54–80, 2015.

[22] Suncica Canic, Josip Tambača, Giovanna Guidoboni, Andro Mikelić, Craig J. Hartley, and Doreen Rosenstrauch. Modeling viscoelastic behavior of arterial walls and their interaction with pulsatile blood flow. *SIAM J. Appl. Math.*, 67(1):164–193, 2006.

[23] P. Causin, J.F. Gerbeau, and F. Nobile. Added-mass effect in the design of partitioned algorithms for fluid-structure problems. *Comput. Methods Appl. Mech. Engrg*, 194(42-44):4506–4527, 2005.

[24] M. Cervera, R. Codina, and M. Galindo. On the computational efficiency and implementation of block-iterative algorithms for nonlinear coupled problems. *Engrg. Comput.*, 13(6):4–30, 1996.

[25] Jan Cesenek, Miloslav Feistauer, and Adam Kosik. An arbitrary LagrangianEulerian discontinuousGalerkin method for simulations of flows over variable geometries. *Journal of Fluids and Structures*, pages 312–329, 2010.

[26] L.A. Charles, W.R. Jeffrey, I.B. Edward, and A.P. Robert. Experimental investigation of steady flow in rigid models of abdominal aortic aneurysms. *Annals of Biomedical Engineering*, 23(1):29–39, 1995.

[27] B. Cockburn, G. Kanschat, and D. Schötzau. A locally conservative LDG method for the incompressible Navier Stokes equations. *Math. Comput.*, 74:1067–1095, 2005.

[28] B. Cockburn and C. W. Shu. The local discontinuous Galerkin finite element method for convection-diffusion systems. *SIAM J. Numer. Anal.*, pages 2440–2463, 1998.

[29] G.H. Cottet, E. Maitre, and T. Milcent. Eulerian formulation and level set models for incompressible fluid-structure interaction. *Mathematical Modelling and Numerical Analysis*, 42(3):471–492, 2008.

[30] S. Deparis, M. Discacciati, G. Fourestey, and A. Quarteroni. Fluid-structure algorithms based on Steklov-Poincaré operators. *Comput. Methods Appl. Mech. Engrg.*, 195:5797–5812, 2006.

[31] S. Deparis, M.A. Fernandez, and L. Formaggia. Acceleration of a fixed point algorithm for a fluid-structure interaction using transpiration condition. *Math. Model. Numer. Anal.*, 37(4):601–616, 2003.

[32] Jean Donéa. A Taylor-Galerkin method for convective transport problems. In *Numerical methods in laminar and turbulent flow (Seattle, Wash., 1983)*, pages 941–950. Pineridge, Swansea, 1983.

[33] M. Dubiner. Spectral methods on triangles and other domains. *J. Sci. Comput.*, 6:345–390, 1991.

[34] H. Fang, Z. Wang, Z. Lin, and M. Liu. Lattice Boltzmann method for simulating the viscous flow in large distensible blood vessels. *Phys. Rev. E*, 65:051925.1–051925.11, 2002.

[35] L.J. Fauci and R. Dillon. Biofluidmechanics of reproduction. *Ann. Rev. Fluid Mech.*, 38:371–394, 2006.
[36] Z.-G. Feng and E.E. Michaelides. The immersed boundary-lattice Boltzmann method for solving fluidparticles interaction problem. *J. Comp. Phys.*, 195(2):602–628, 2004.
[37] M.A. Fernández, J.F. Gerbeau, and C. Grandmont. A projection algorithm for fluid-structure interaction problems with strong added-mass effect. *Comptes Rendus Mathematique*, 342(4):279–284, 2006.
[38] Miguel Angel Fernández. Incremental displacement-correction schemes for incompressible fluid-structure interaction. *Numerische Mathematik*, 123(1):21–65, 2013.
[39] E. Ferrer and R.H.J. Willden. A high order discontinuous Galerkin finite element solver for the incompressible Navier-Stokes equations. *Comput. Fluids*, 46:224–230, 2011.
[40] C. Figueroa, I. Vignon-Clementel, K.E. Jansen, T. Hughes, and C. Taylor. A coupled momentum method for modeling blood flow in three-dimensional deformable arteries. *Comput. Methods Appl. Mech. Eng.*, 195:5685–5706, 2006.
[41] E.A. Finol and C.H. Amon. Blood flow in abdominal aortic aneurysms: pulsatile flow hemodynamics. *J Biomech Eng.*, 123(5):474–84, 2001.
[42] A.L. Fogelson and R.D. Guy. Platelet-wall interactions in continuum models of platelet thrombosis: Formulation and numerical solution. *Math. Med. Biol.*, 21:293–334, 2004.
[43] L. Formaggia, J. Gerbeau, F. Nobile, and A. Quarteroni. On the coupling of 3d and 1d Navier-Stokes equations for flow problems in compliant vessels. *Comput. Methods Appl. Mech. Eng.*, 19:561–582, 2001.
[44] M. Israeli G. Karniadakis and S. Orszag. High-order splitting methods for the incompressible Navier-Stokes equations. *Journal of Computational Physics*, 97:414–443, 1991.
[45] J.F. Gerbeau and M. Vidrascu. A quasi-Newton algorithm based on a reduced model for fluid-structure interactions problems in blood flows. *Math. Model. Numer. Anal.*, 37(4):631–648, 2003.
[46] D. Gottlieb1977 and S.A. Orszag. Numerical analysis of spectral methods: Theory and applications. *Regional conference series in applied mathematics*, 1977.
[47] B.E. Griffith, R.D. Hornung, D.M. McQueen, and C.S. Peskin. An adaptive, formally second order accurate version of the immersed boundary method. *J Comput Phys.*, 223:10–49, 2007.
[48] G. Guidoboni, N. Cavallini, R. Glowinski, S. Canic, and S. Lapin. A kinematically coupled time-splitting scheme for fluid-structure interaction in blood flow. *Applied Mathematics Letters*, 22(5):684–688, 2009.
[49] Giovanna Guidoboni, Roland Glowinski, Nicola Cavallini, and Suncica Canic. Stable loosely-coupled-type algorithm for fluid-structure interaction in blood flow. *J. Comput. Phys.*, 228(18):6916–6937, 2009.
[50] J. Hesthaven and T. Warburton. *Nodal discontinuous Galerkin methods: Algorithms, analysis, and applications*. Springer, 2008.
[51] T. J. R. Hughes, W. K. Liu, and T. K. Zimmermann. Lagrangian-Eulerian finite element formulation for incompressible viscous flows. *Computer Methods in Applied Mechanics and Engineering*, 29(3):329–349, 1981.
[52] Anna Hundertmark-Zaušková, Mária Lukáčová-Medvidová, and Gabriela Rusnáková. Fluid-structure interaction for shear-dependent non-Newtonian fluids. In *Topics in mathematical modeling and analysis*, volume 7 of *J. Nečas Cent. Math. Model. Lect. Notes*, pages 109–158. Matfyzpress, Prague, 2012.
[53] V. John. Reference values for drag and lift of a two dimensional time-dependent flow around a cylinder. *Int. J. Numer. Meth. Fluids*, 44:777–788, 2004.
[54] G. Karniadakis and S. Sherwin. *Spectral/hp Element Methods for Computational Fluid Dynamics*. Oxford, 2005.
[55] M. Krafczyk, M. Cerrolaza, M. Schulz, and E. Rank. Analysis of 3D transient blood flow passing through an artificial aortic valve by lattice-boltzmann methods. *J Biomech.*, 31(5):453–462, 1998.
[56] M. Krafczyk, J. Tolke, E. Rank, and M. Schulz. Two-dimensional simulation of fluid-structure interaction using lattice-Boltzmann methods. *Comput. Struct.*, 79:2031–2037, 2001.
[57] U. Küttler and W.A. Wall. Fixed-point fluid-structure interaction solvers with dynamic relaxation. *Computational Mechanics*, 43(1):61–72, 2008.
[58] S. Lim and C.S. Peskin. Simulations of the whirling instability by the immersed boundary method. *SIAM J. Sci. Comput.*, 25:2066–2083, 2004.
[59] I. Lomtev, R.M. Kirby, and G.E. Karniadakis. A Discontinuous Galerkin ALE Method for Compressible Viscous Flows in Moving Domains. *Journal of Computational Physics*, page 128159, 1999.
[60] C. Farhat M. Lesoinne. Geometric conservation laws for flow problems with moving boundaries and deformable meshes, and their impact on aeroelastic computations. *Comput. Methods Appl. Mech. Eng.*, 134:7190, 1996.
[61] H. Matthies and J. Steindorf. Numerical efficiency of different partitioned methods for fluid-structure interaction. *Z. Angew. Math. Mech.*, 2(80):557–558, 2000.
[62] L.A. Miller and C.S. Peskin. A computational fluid dynamics study of 'clap and fling' in the smallest insects. *J. Exp. Biol.*, 208(2):195–212, 2005.
[63] D.P. Mok and W.A. Wall. Partitioned analysis schemes for transient interaction of incompressible flows and nonlinear flexible structures. In *Trends in computational structural mechanics (W.A. Wall, K.U. Bletzinger and K. Schweizerhof, Eds.)*, CIMNE, Barcelona, Spain, 2001.
[64] F. Nobile. Numerical approximation of fluid-structure interaction problems with application to hemodynamics. *Ph.D. thesis EPFL*, 2001.
[65] F. Nobile and C. Vergara. An effective fluid-structure interaction formulation for vascular dynamics by generalized Robin conditions. *SIAM J. Sci. Comput.*, 30:731–763, 2008.
[66] K. Ouriel, R.M. Green, C. Donayre, C.K. Shortell, J. Elliott, and J.A. DeWeese. An evaluation of new methods of expressing aortic aneurysm size: relationship to rupture . *Journal of vascular surgery*, 15:12–20, 1992.
[67] R.A. Peattie, C.L. Asbury, E.I. Bluth, and J.W. Ruberti. Steady flow in models of abdominal aortic aneurysms. part i:

Investigation of the velocity patterns. *J Ultrasound Med.*, 15(10):679–88, 1996.
[68] R.A. Peattie and E.I. Bluth. Experimental study of pulsatile flows in models of abdominal aortic aneurysms. *Proceedings of the 20th Annual International Conference of the IEEE Engineering in Medicine and Biology Society*, 20(1), 1998.
[69] P.O. Persson, J. Bonet, and J. Peraire. Discontinuous Galerkin solution of the Navier-Stokes equations on deformable domains. *Computer Methods in Applied Mechanics and Engineering*, page 15851595, 2009.
[70] C. Peskin and D.M. McQueen. A three-dimensional computational method for blood flow in the heart i. immersed elastic fibers in a viscous incompressible fluid. *J. Comput. Phys.*, 81(2):372–405, 1989.
[71] C. S. Peskin. The immersed boundary method. *Acta Numer.*, 11:479–517, 2002.
[72] A. Quaini. Algorithms for fluid-structure interaction problems arising in hemodynamics. *Ph.D. thesis EPFL*, 2009.
[73] A. Quaini and A. Quarteroni. A semi-implicit approach for fluid-structure interaction based on an algebraic fractional step method. *Math. Models Methods Appl. Sci.*, pages 957–985., 2007.
[74] A. Quarteroni, R. Sacco, and F. Saleri. *Numerical Mathematics*. Springer Verlag, 2007.
[75] A. Quarteroni, M. Tuveri, and A. Veneziani. Computational Vascular Fluid Dynamics: Problems, Models and Methods. *Comput. Vis. Science*, 2:163–197, 2000.
[76] A. Quarteroni and A. Valli. *Numerical approximation of partial differential equations*. Springer, 1997.
[77] A. Quarteroni and A. Valli. *Domain Decomposition Methods for Partial Differential Equations*. Oxford Science Publications, 1999.
[78] B. Cockburn S. Rhebergen. A spacetime hybridizable discontinuous Galerkin method for incompressible flows on deforming domains. *Journal of Computational Physics*, 231:4185–4204, 2012.
[79] M. Schäfer, S. Turek, F. Durst, E. Krause, and R. Rannacher. *Benchmark computations of laminar flow around a cylinder*. 1996.
[80] K. Shahbazi. An explicit expression for the penalty parameter of the interior penalty method. *Journal of Computational Physics*, 205:401407, 2005.
[81] K. Shahbazi, P.F. Fischer, and C.R. Ethier. A high-order discontinuous Galerkin method for the unsteady incompressible Navier-Stokes equations. *J. Comput. Phys.*, 222:391–407, 2007.
[82] Eduardo Soudah, F.Y.K. Ng, T.Loong, Maurizio Bordone, Uei Pua, and Sriram Narayanan. CFD modelling of abdominal aortic aneurysm on hemodynamic loads using a realistic geometry with CT . *Computational and Mathematical Methods in Medicine*, Article ID 472564, 2013.
[83] R. van Loon, P. Anderson, J. de Hart, and F. Baaijens. A combined fictitious domain/adaptive meshing method for fluid-structure interaction in heart valves. *Int. J. Num. Meth. Fluids*, 46:533–544, 2004.
[84] M. Zhang and C. W. Shu. An analysis of three different formulations of the discontinuous galerkin method for diffusion equations. *Math. Models Methods Appl. Sci.*, 13:395–413, 2003.
[85] S.Z. Zhao, X.Y. Xu, and M.W. Collins. The numerical analysis of fluid-solid interactions for blood flow in arterial structures Part 2: development of coupled fluid-solid algorithms. *Proc. Instn. Mech. Engrs. Part H*, 212:241–252, 1998.